Journal of Physics B: Atomic,
Molecular and Optical Physics

**TUTORIAL** • **OPEN ACCESS**

# Introduction to macroscopic power scaling principles for high-order harmonic generation

To cite this article: C M Heyl *et al* 2017 *J. Phys. B: At. Mol. Opt. Phys.* **50** 013001





OPEN ACCESS
IOP Publishing
Journal of Physics B: Atomic, Molecular and Optical Physics
J. Phys. B: At. Mol. Opt. Phys. **50** (2017) 013001 (21pp)
doi:10.1088/1361-6455/50/1/013001

Tutorial

# Introduction to macroscopic power scaling principles for high-order harmonic generation

**C M Heyl[1,2], C L Arnold[1], A Couairon[3] and A L'Huillier[1]**

[1] Department of Physics, Lund University, PO Box 118, SE-22100 Lund, Sweden
[2] JILA, NIST and the University of Colorado, 440 UCB, Boulder, CO 80309, USA
[3] Centre de Physique Théorique, École Polytechnique, CNRS, F-91128, Palaiseau, France

E-mail: christoph.heyl@fysik.lth.se

Received 9 April 2015, revised 10 August 2016
Accepted for publication 26 August 2016
Published 6 December 2016

**Abstract**

This tutorial presents an introduction to power scaling concepts for high-order harmonic generation (HHG) and attosecond pulse production. We present an overview of state-of-the-art HHG-based extreme ultraviolet (XUV) sources, followed by a brief introduction to basic principles underlying HHG and a detailed discussion of macroscopic effects and scaling principles. Particular emphasis is put on a general scaling model that allows the invariant scaling of the HHG process both, to $\mu$J-level driving laser pulses and thus to multi-MHz repetition rates as well as to 100 mJ-or even Joule-level laser pulses, allowing new intensity regimes with attosecond XUV pulses.

Keywords: high-order harmonic generation, phase matching, attosecond science, scale-invariance, nonlinear optics

(Some figures may appear in colour only in the online journal)

List of abbreviations

| | |
|---|---|
| CEP | Carrier-to-envelope phase |
| CPA | Chirped pulse amplification |
| CW | Continuous wave |
| HHG | High-order harmonic generation |
| IAP | Isolated attosecond pulse |
| NA | Numerical aperture |
| NCHHG | Noncollinear HHG |
| OPA | Optical parametric amplification/amplifier |
| OPCPA | Optical parametric chirped pulse amplification/amplifier |
| SFA | Strong field approximation |
| UV | Ultraviolet (~380–200 nm) |
| VUV | Vacuum ultraviolet (~200–100 nm) |
| XUV | Extreme ultraviolet (~100–10 nm) |



## 1. Introduction

During the last decades, coherent extreme ultraviolet (XUV) sources based on high-order harmonic generation (HHG) have become indispensable tools in different research fields, most of them focusing on basic research within atomic, molecular and optical physics [1–5] but including areas like

precision frequency metrology [6] and applied microscopy [7]. As the spectral coverage of conventional laser sources does not extend far into the ultraviolet (UV) spectral region, frequency conversion processes are needed to access the XUV spectral region with coherent table-top sources. While perturbative nonlinear optical wave mixing processes in bulk materials and/or gases give access to the vacuum ultraviolet (VUV) and the mid-infrared spectral region, the HHG process opens the door into the the XUV and beyond and allows the generation of attosecond pulses.

Attosecond pulse generation via HHG[4] in gases forms the basis for attosecond science, a growing field in optical sciences. Today's HHG-based XUV sources can provide laser-like pulses with excellent spatial and temporal coherence properties [8–12], with photon energies reaching into the soft-x-ray spectral region [13, 14] and pulse durations from several 100 fs down to 100 as [15]. These remarkable properties enable to probe ultrafast electronic processes like ionization dynamics [16–18], or charge migration in complex systems [4]. They also allow ultrahigh precision measurements of narrow transitions in the XUV [6, 19] and provide new possibilities for nano-scale imaging [20–22].

In spite of many exciting results HHG-based XUV sources have enabled already, they suffer from one main obstacle: the relatively low photon flux available in the XUV. The average power of a single harmonic above 20 eV of state-of-the-art sources approaches 1 mW [19, 23, 24] with repetition rates exceeding 200 MHz [25]. On the other hand, pulse energies reaching 1 $\mu$J [26, 27] have been achieved at low repetition rate (10 Hz). However, many applications would benefit greatly from a higher average power. Recent efforts within the still young field of attosecond science reveal two important development directions, setting demands on future attosecond source technology: first, the production of very energetic attosecond pulses, with the aim to develop pump–probe schemes with intense attosecond pulses, thus opening nonlinear optics processes to the XUV and attosecond regimes; second, high repetition rate, high average power attosecond sources, with applications to ultrafast studies of solid state systems and correlated electron dynamics as well as for new imaging schemes employing XUV table-top light sources.

In this tutorial, we address these two source development directions, focusing on the scaling of HHG-based XUV sources towards higher repetition rates, pulse energies and average powers. We mainly concentrate on the technological possibilities and requirements set by the HHG process itself and include a brief discussion of current laser development efforts along these lines. We give an overview of state-of-the-art HHG sources and discuss in detail a general scaling model [28], which allows the scaling of HHG and attosecond pulse generation in pulse energy, repetition rate and average power while keeping the main characteristic XUV pulse parameters invariant. With today's laser technology, an invariant XUV source scaling can be performed over more than six orders of magnitude with no upper limit for the XUV pulse energy and average power, provided that appropriate driving laser sources become available.

Substantial parts of this tutorial are based on the PhD Thesis of the first author [29] as well as on [28].

### *1.1. Outline of this tutorial*

This tutorial is divided into three sections. Section 2 starts with a brief historical perspective on HHG-based XUV source development, followed by an overview of today's HHG-sources and their driving laser technology. Sections 3 provides a brief introduction to the basic mechanisms of HHG and related macroscopic propagation phenomena, which are essential for the discussion of HHG scaling principles. We start with a phenomenological discussion of basic propagation effects using commonly applied terminology. A more rigorous discussion of macroscopic propagation phenomena leading to general scaling principles based on nonlinear wave equations is presented in section 4, followed by user-friendly guidelines and a brief discussion of different HHG generation schemes. The section concludes with a discussion of the consequences and possibilities for HHG sources enabled by the scale-invariance of the HHG process. We conclude with a brief summary and an outlook on current high harmonic source development directions.

## 2. HHG-based XUV sources: characteristic properties and state-of-the-art

### *2.1. HHG source development—a brief historical perspective*

The HHG process was discovered in 1987, when researchers in France and in the United States observed a plateau of weak, odd order harmonics extending into the XUV when a picosecond laser was focused into a gas target [30, 31]. The underlying physical mechanisms could be described with a simple model (see section 3.1) and it was soon predicted that this process should allow the generation of attosecond pulses [32, 33]. However, it took fourteen years to demonstrate experimentally the formation of attosecond pulse trains [34] and isolated attosecond pulses (IAPs) [35].

During the last decades, a continuous development of HHG-based XUV source technologies has led to unprecedented parameters provided by today's sources. In the first years after the discovery of HHG, strong efforts were aimed to temporally characterize and isolate the generated attosecond pulses. Following this ground work, the extension of the photon energy cutoff into the keV regime [13, 36] and the first demonstration of a frequency comb in the VUV enabled by HHG inside an enhancement cavity [37, 38] mark major breakthroughs for HHG source development. Today's challenges include the extension of the spectral range, both further into the x-ray regime as well as (for isolated attosecond and few-fs XUV and VUV pulses) into the VUV, the

[4] Note that the term HHG is used in this tutorial for the process that leads to harmonic emission with energies above the ionization threshold of the atom, forming attosecond pulse trains in the time domain. We also include the generation of isolated attosecond pulses although, in this case, the spectral content typically does not show a harmonic comb structure.

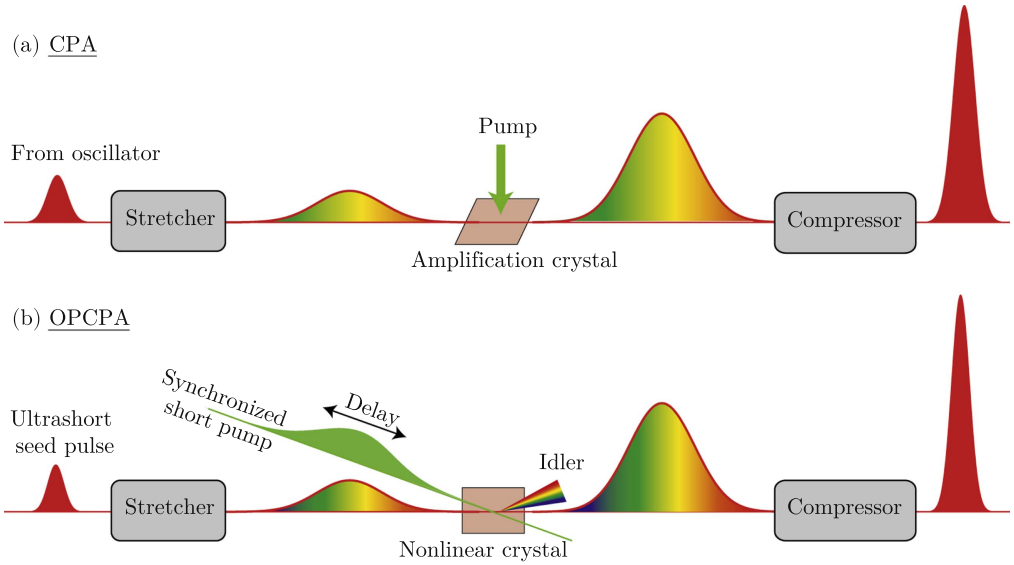


**Figure 1.** (a) Principle of chirped pulse amplification: to avoid damage and nonlinear effects during amplification, the seed pulses, usually obtained from a Kerr-mode-locked ultrashort pulse oscillator, are stretched from femtosecond duration to tens to hundreds of picoseconds, amplified and afterwards re-compressed close to transform-limited duration. (b) Principle of optical parametric chirped pulse amplification: ultrashort seed pulses, stretched to approximately match the pump pulse duration, are amplified by nonlinear mixing with an intense synchronized, usually picosecond duration, pump pulse. Afterwards the pulse is re-compressed close to the transform limit.

development of new methods for IAP generation, the increase of photon flux as well as the exploration of new generation schemes including surface- and solid-state-based HHG. While the first high-order harmonics and/or attosecond pulses have been generated in a simple gas jet (or gas cell), other methods have been investigated, including the generation in gas-filled capillaries [39] as well as from plasma surfaces [40] and solids [41]. Other approaches point towards the generation sub-1fs light pulses via broadband light-field synthesis [42] and new pulse post-compression techniques [43].

Although novel generation schemes like surface and solid-state based HHG offer promising perspectives (e.g. a higher photon flux and new insight into solid-state electron dynamics), these techniques are not yet well established and attosecond pulses using these generation processes have not yet been fully characterized. In this tutorial, we focus on well-established technology, i.e. gas-based HHG sources.

### *2.2. Driving laser sources for HHG*

Today, the most widely used lasers to drive HHG and attosecond sources are based on titanium:sapphire (Ti:sapphire) as laser active material, providing intense femtosecond pulses centered around 800 nm carrier wavelength. In the early days of HHG, a variety of lasers were employed and the first experiments were performed with a sub-picosecond $KrF^*$ eximer laser at 248 nm [30] and a Nd:YAG laser emitting 36 ps pulses at 1064 nm [31]. Shortly after, other experiments used sub-picosecond dye lasers in the visible spectral range at 616 nm [44, 45] as well as fundamental (1053 nm) and frequency doubled Nd:glass lasers [45, 46].

In the late 1980-ties Ti:sapphire emerged as new solid-state laser material [47] with an exceptional amplification bandwidth. Together with the development of the Kerr-lens mode-locking technique [48] and the invention of chirped pulse amplification (CPA) [49], the generation and amplification of ultrashort laser pulses became much easier. The principle of CPA is highlighted in figure 1(a).

The first commercial Ti:sapphire femtosecond lasers were readily available in the early nineties with peak powers up to the TW level. The new technology was picked-up rapidly by the HHG community and the first high-order harmonics generated from Ti:sapphire lasers followed shortly after [50–53]. Due to its performances as well as further technological innovations, such as the generation of few-cycle pulses by post-compression in hollow capillaries [54] and the stabilization of the carrier-to-envelope phase (CEP) [55], Ti:sapphire rapidly became the dominating technology for HHG. The first demonstrations of attosecond pulse trains and single attosecond pulses were performed with Ti:sapphire technology [34, 35]. The Ti:sapphire lasers commonly employed for HHG today have repetition rates in the range of 10 Hz to 10 kHz, pulse duration between 20 and 40 fs, with possibility to compress down to 5 fs, pulse energy from a fraction of a mJ to hundreds of mJ, and average power up to tens of Watts.

The dominance of Ti:sapphire for HHG is recently being challenged by a number of important developments such as optical parametric chirped pulse amplification (OPCPA), CPAs based on ytterbium-doped (Yb) gain materials as well as high-average power and high energy Yb oscillators. The driving force for establishing new laser technology for HHG is to overcome some of the limitations inherent to Ti:sapphire, such as the difficult thermal management for high average power and high repetition rate, the limited amplification bandwidth that makes it difficult to reach pulse duration below ~20 fs and the fixed carrier wavelength close to 800 nm. The last point is often addressed by optical parametric amplifiers (OPAs) [56–59] that can be used to shift the

driving laser wavelength for HHG over the entire visible to the mid-infrared spectral range. OPAs are powerful and straight-forward expansions of the wavelength range. They also open up for attosecond pulses in the soft-x-ray spectral range by the wavelength scaling of HHG [58, 60–62]. However, OPAs driven by Ti:sapphire lasers do not allow a higher average power or higher repetition rate.

An alternative to Ti:sapphire driven OPAs are OPCPAs. Here ultrashort seed pulses are stretched and amplified by nonlinear mixing with intense picosecond pulses in a nonlinear crystal. The nonlinear mixing is a three wave interaction, similar to difference frequency generation, between a pump wave with photon energy $\omega_P$, a signal wave with frequency $\omega_s$ and an idler wave with frequency $\omega_i$, where $\omega_P = \omega_s + \omega_i$ and $\omega_s > \omega_i$. For efficient amplification the process must be phase-matched, i.e. the corresponding wave vectors need to fulfill $k(\omega_P) - k(\omega_s) - k(\omega_i) = 0$. The amplification can be seeded either by the signal or the idler wave; the other wave is generated in the mixing process. Unlike conventional laser amplification, where a laser active material is pumped and the energy difference between the pump photons and the laser photons, i.e. the quantum defect, is dissipated thermally, there are only virtual levels involved in OPA. This greatly simplifies thermal management issues and when combined with powerful picosecond pump lasers, high-average power and high-repetition rate pulses can be produced. Furthermore, OPCPAs can be realized in wavelength ranges where no convenient laser materials exist, e.g. in the short-wavelength infrared and mid-infrared regions, and in particular cases, phase-matching bandwidths can be achieved that directly allow for the amplification of few-cycle laser pulses without the need for sophisticated post-compression [63, 64]. The principle of OPCPA is illustrated in figure 1(b). The first OPCPA was demonstrated in the beginning of the nineties [65], but the technique has benefited greatly from recent advances in Yb-doped CPA lasers, providing high power pump lasers [66].

Today, several different Yb laser architectures based on fiber amplifiers [67], slab amplifiers [68] and thin-disk amplifiers [69] can deliver hundreds of Watts at repetition rates ranging from kHz to MHz for efficient OPCPA pumping. If the seed is stretched to tens of picoseconds, also pump lasers based on Neodymium-doped gain materials can be used. OPCPAs have been developed from the visible to the mid-infrared spectral range [70–78] and are today routinely used in HHG [13, 79–81].

While, as described above, CPAs based on Yb-doped material gained large importance as OPCPA pumps, these lasers with sub-picosecond pulses at 1030 nm, are also used to directly drive HHG [82–84]. The Yb architecture has a number of advantages compared to Ti:sapphire. While for Ti:sapphire pumping sophisticated and expensive frequency-doubled Q-switched green pump lasers are needed, Yb-doped gain materials can be directly pumped with high-power diode-lasers around 910 or 975 nm. The small quantum defect makes thermal management less demanding and the long upper-state lifetime enables continuous-wave (CW) pumping. This allows for compact and economical Yb-based CPAs with good efficiency, average power of tens to hundreds of Watts and scalability to kW average power. Despite these clear benefits, the relatively narrow gain bandwidth (compared to Ti:sapphire) currently does not allow for pulse duration much below ~200 fs. However, with pulse post-compression techniques based on gas-filled hollow capillaries [54] or hollow core Kagomé fibers [85] sub-50 fs pulse durations were recently achieved from Yb fiber CPAs and used for HHG [86]. With two compression stages even the few-cycle regime is accessible [87].

The last trend that should be highlighted here is to completely disregard amplification and stretching and to drive HHG directly from a laser oscillator. The concept has been demonstrated first using a commercial Ti:sapphire oscillator [88], but benefits greatly from recent developments in Yb thin-disk oscillators, which can achieve at least two orders of magnitude higher average power. Current record values are at more than 10 $\mu$J pulse energy, some hundred femtoseconds pulse duration and almost 300 W of average power. The development points towards the kW average power level [89, 90]. Combined with external pulse compression in hollow-core fibers [91–93] high-power Yb thin disk oscillators are promising drivers for high repetition rate (tens of MHz) future HHG sources [94].

### 2.3. Today's HHG-based XUV source technology

*2.3.1. Source characteristics.* The basic principles underlying a typical HHG-source are schematically illustrated in figure 2(a). An ultrashort laser pulse is focused into a gas target to intensities in the range of $10^{13}$–$10^{15}$ W cm$^{-2}$. At these intensities, high-harmonic emission occurs (see also section 3) and XUV light is emitted collinearly (in most cases) along the driving laser field propagation direction. Although many state-of-the-art HHG-based XUV sources are based on rather simple schemes, as the one depicted in figure 2(a), a multitude of variations exits, involving e.g. different gas medium configurations, different driving laser pulse properties and different schemes allowing spectral filtering [34, 95, 96] and/or splitting and delaying [26, 97–100] the generated XUV pulses. Furthermore, especially for HHG sources operating at multi-MHz repetition rates, concepts involving HHG inside a femtosecond enhancement cavity have been demonstrated [37, 38, 101].

Despite the variety of concepts employed today, most HHG-based XUV sources provide XUV pulses with common characteristics in the spectral (see figure 2(b)), temporal (see figure 2(c)) and spatial domains, as summarized below.

Because of the temporal coherence properties of the generated XUV light, trains of ultra-short pulses with duration below one femtosecond are formed during the HHG process (for driving laser pulse with several optical cycles). In the spectral domain, this pulse structure corresponds to a comb of harmonics of the fundamental driving field central frequency. In contrast, an IAP, which can be generated for example by restricting the XUV emission to a single half-cycle of the fundamental field [15, 35] or by selecting only a single XUV pulse out of a spatially dispersed pulse train [102, 103], has a

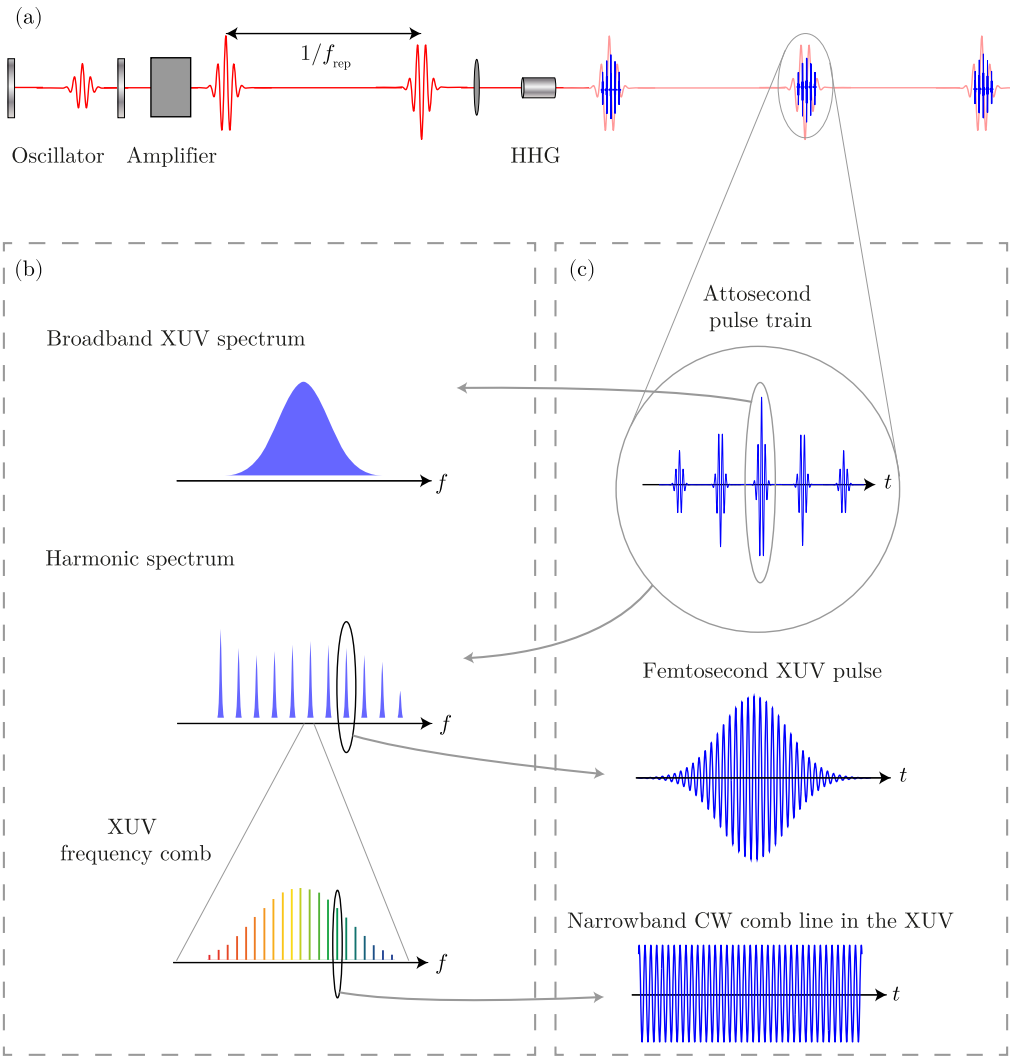


**Figure 2.** Schematic overview of a typical HHG source (a) and the characteristic properties of the generated XUV pulses in spectral (b) and temporal (c) domain. Note that usually not all displayed characteristics are provided by one single HHG source (see text for details). $f_{\mathrm{rep}}$ denotes the repetition rate.

continuous spectral content. Both attosecond pulse trains and IAPs allow measurements of ultrafast processes such as ionization [16–18] or charge migration dynamics [4]. Often, interferometric pump–probe schemes [104] are employed for such measurements.

The spectral selection of a single harmonic via band-pass optics or monochromators allows extracting a few-femtosecond XUV pulse (the exact duration depends on the duration of the driving laser field) with relatively narrow spectral content of typically a few 100 meV. Such pulses have very similar temporal and spectral properties as femtosecond laser pulses but enable to reach photon energy regimes that are otherwise not accessible with table-top laser technology. Especially applications within surface-and solid-state physics can benefit from XUV sources delivering such pulses as they provide, for example, access to the entire Brillouin zone [105–108]. For such applications, a high pulse energy leads rapidly to space charge effects. Low pulse energies and high repetition rates are thus needed to improve statistics while minimizing space charge.

Another interesting property that HHG-based XUV sources can provide is the frequency comb-structure, which can be transferred from the driving laser into individual harmonics if the employed driving laser has frequency-comb properties [37, 38]. In this case, each harmonic order consists of thousands of spectrally narrow CW lines. As a high repetition rate is beneficial for reaching the temporal coherence required to form a frequency comb, average power limitations have so far restricted XUV-comb generation to enhancement-cavity based approaches. In this scheme, a passive enhancement cavity is used to boost the average power available to drive HHG (see e.g. [109] for details). XUV frequency combs allow for the first time ultra-high precision frequency measurements in the XUV spectral region [6] where for example highly charged ions or possibly nuclear transitions are targets of interest.

Last but not least, the excellent spatial coherence properties of the XUV pulses generated via HHG open up new possibilities for lens-less high-resolution imaging [20, 22]. Because of the short wavelength, a high-spatial resolution can

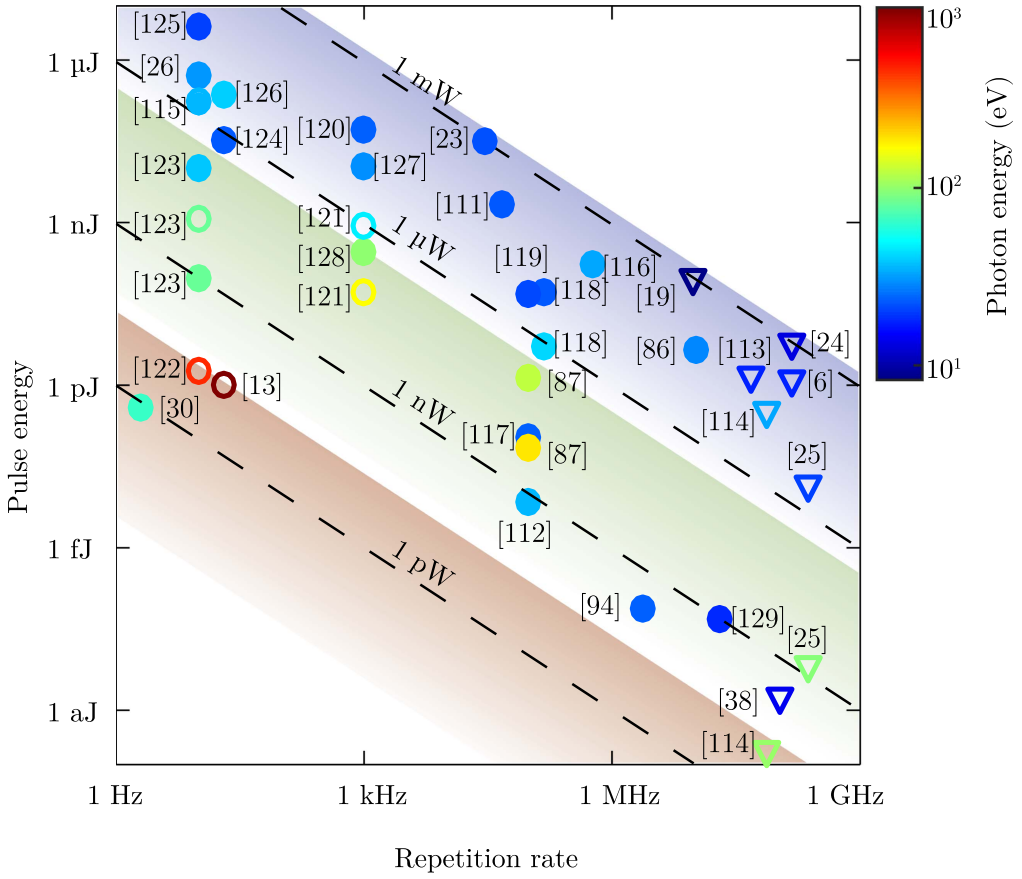


**Figure 3.** Pulse energy, repetition rate and average power (dashed lines) of state-of-the-art HHG-based XUV sources. Three different types of HHG sources are displayed: single-pass HHG in a gas cell, gas jet or similar (filled circles), single-pass HHG in a capillary (open circles) and intra-cavity HHG (triangles). The displayed values refer to pulse energy and average power within a single harmonic order or a spectral bandwidth of $2\omega_0$ for spectral continua. The shaded areas indicate the average power of the reported best-values within three different photon energy ranges ($\geqslant$20 eV, $\geqslant$100 eV and $\geqslant$1 keV), as indicated by the color. Reference list: [6, 13, 19, 23–26, 30, 38, 86, 87, 94, 111, 115, 113, 114, 116, 117, 112, 118–129].

be reached while the spatial coherence enables to apply lensless imaging schemes in spectral regions where the application of conventional optical imaging elements is difficult.

*2.3.2. Overview of state-of-the-art sources.* Today a wide range of laser parameters is used to drive HHG-based XUV sources, with pulse durations from several hundred femtoseconds to the few-cycle regime, pulse energies from the $\mu$J to the 100 mJ level, and repetition rates from a few Hz to hundreds of MHz for enhancement cavities. Ti:sapphire CPAs with wavelengths around 800 nm and recently also Yb-based CPAs around 1030 nm are commonly used (see section 2.2). At the same time, mid-infrared sources spanning down to 4 $\mu$m have enabled pushing HHG-based XUV generation into new photon energy regimes [13]. Also, wavelength-scaling approaches employing short wavelength drivers have been recently revisited [110, 111], shedding new light on short-wavelength scaling and thus onto the early days of HHG [45].

Figure 3 provides an overview of state-of-the-art HHG-based XUV sources. We also include a few historically important sources showing data points representing one of the first high-harmonic spectra observed [30], the first HHG spectrum measured at a 100 kHz repetition rate [112] as well as one of the first intra-cavity high harmonic signals reported [38]. Each data point shows pulse energy, repetition rate, average power and photon energy of the generated[5] spatially and spectrally integrated harmonic signal of a single harmonic order. Note that the real power levels available at the experiment are typically lower as losses due to spectral filtering and, for intra-cavity HHG, due to out-coupling have to be considered. For continuous XUV emission, the integrated bandwidth is $2\omega_0$ with $\omega_0$ denoting the fundamental laser angular frequency. The data points were selected by choosing characteristic best values as e.g. the highest average power per harmonic within the measured spectral range or the average power close to the cut-off. The figure displays data points for single pass HHG sources employing gas jets and cells (filled circles), capillaries (open circles) and intra-cavity HHG systems (triangles).

The average power values shown in figure 3 are determined by two factors, the laser average power and the

[5] Depending on the method employed for calibrating the measured signal, the displayed generated signal is either an estimated value taking losses along the optical path from the generation to the detection into account, or, in some cases where only the measured value was reported (e.g. [25, 113, 114]), we show the detected signal.

conversion efficiency into the XUV. However, as most driving laser sources employed for HHG operate at an average power around 100 mW to a few Watts, the displayed XUV pulse energy and average power values give an approximate indication for the conversion efficiencies reached. For high-power intra-cavity sources (e.g. [6, 24]) as well as for recent single-pass high-repetition rate results [86, 118] (see also [130]) a laser average power above 50 W has been employed while early results as e.g. [30] have been obtained with much less powerful laser systems.

Figure 3 shows several characteristic trends. Today, the highest average power single-pass sources reach values between 100 $\mu$W and 1 mW over nearly the entire repetition rate range reported. This trend has only been achieved recently. Before 2011, the reported average power values reached more than 10 $\mu$J for 10 Hz and 1 kHz systems but a rapid decrease could be observed towards higher repetition rates. This trend was explained by increasing difficulties to phase match the HHG process at high repetition rates where only $\mu$J-level laser pulse energies could be delivered, implying tight focusing geometries and small interaction volumes [109, 112]. In 2011, studies of HHG phase matching indicated that phase-matched generation was possible even under tight focusing geometries [117]. These predictions were analyzed in more detail and verified experimentally by Rothhardt and co-workers [118], showing that conversion efficiencies close to the best values reported for 1kHz sources could be achieved even for tight focus HHG. Recently, a more general model for energy and power scaling of nonlinear optical processes in gases was developed. The model supports these earlier results, bringing them into a broader context and allowing predictions for further energy-, power- and repetition rate scalability (see section 4).

Figure 3 also allows a comparison between different source types. Intra-cavity sources currently dominate the high average power regime for the photon energy range around 20 eV. The explanation is less straight-forward than it might seem. Because of the promising approach to superimpose each laser pulse after HHG with the next pulse from the driving laser, an effective power enhancement is possible and an increased XUV power seems realistic. However, due to limitations arising from maintaining a high power-enhancement while driving a very nonlinear process inside the cavity, the intra-cavity frequency conversion efficiencies reported today are well below the best values for single-pass HHG. However, recent results point towards a possible solution of this problem [24, 131] and only very recently, an intra-cavity HHG system allowed to convert the pumping laser power sent into the enhancement cavity more efficiently into the XUV than single pass-schemes at similar driving wavelength [24].

For capillary based HHG sources and jet/cell based sources, similar power levels are reported in the photon energy range up to 100 eV. In contrast, the high photon energy regime above 200 eV is clearly dominated by capillary based sources. For high photon energies where the absorption length for the emitted XUV radiation is typically much longer than for photon energies closer to the ionization potential of the atom, capillary-based HHG has a clear advantage compared to cell- and jet-based sources. The guiding effect of the capillary on the driving laser pulse can lead to an increased coherence length for the frequency conversion process. In contrast, at lower photon energies where the absorption length is much shorter, an increased coherence length has only a marginal effect (see also section 3.2).

## 3. Introduction to basic principles of high-order harmonic and attosecond pulse generation

The emission of high-order harmonics and attosecond pulses upon irradiation of a gas medium with an intense laser pulse usually contains a fingerprint of two different physical phenomena: (i) the response of an individual atom to intense laser light and (ii) the influence of macroscopic effects arising due to the propagation of laser and XUV pulses through the partially ionized medium and the interference of XUV light created at different spatial positions. The first phenomenon is usually referred to as the *single atom response*, the second one is often named *macroscopic propagation* or *phase matching effect*. While the next subsection provides a brief introduction to the single atom response, section 3.2 discusses macroscopic propagation effects.

### 3.1. The single-atom response

The generation of optical harmonic frequencies started with the observation of a second harmonic signal soon after the first laser operation had been reported [132]. Those first optical harmonics belong to the regime of perturbative nonlinear optics, with $\epsilon_{\mathrm{ph}} \ll I_{\mathrm{p}}$. Here $\epsilon_{\mathrm{ph}}$ and $I_{\mathrm{p}}$ denote the emitted photon energy and the ionization potential of the atom, respectively. In this regime, the harmonic field strength scales as $E_q \propto E^q$ with $q$ denoting the harmonic order and $E$ the driving laser field. The term HHG usually refers to the regime of above-threshold harmonics ($\epsilon_{\mathrm{ph}} \geqslant I_{\mathrm{p}}$) where several harmonic frequencies form a large plateau with approximately equal amplitude. To fully describe the underlying process, a non-perturbative quantum mechanical model is required [133, 134]. However, even a semi-classical description, the so-called three-step model [135, 136], allows the prediction of important phenomena such as the extension of the harmonic plateau or the occurrence of two emission events per laser half cycle and photon energy. Here, we use the three step model to introduce basic phenomena of HHG. For a quantum mechanical description the reader is referred e.g. to [134].

The three-step model is illustrated in figure 4. An electron leaves the atom via tunnel-ionization (i), it is then accelerated in the laser field (ii) and can recombine when driven back close to the ion (iii). Using simple classical mechanics the motion of an electron in a strong laser field can be calculated, allowing the derivation of the maximum photon energy that can be emitted upon recombination

$$\epsilon_{\mathrm{ph}}^{\mathrm{max}} = I_{\mathrm{p}} + 3.17\, U_{\mathrm{p}}. \qquad (1)$$

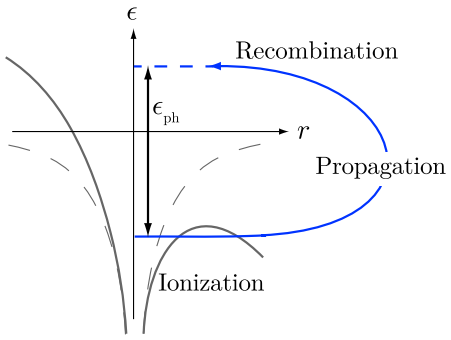


**Figure 4.** The tree-step model of HHG: an electron leaves the atom via tunnel-ionization through the deformed Coulomb barrier, being accelerated in the laser field and, depending on the time of tunneling, driven back to the ion where it may recombine, emitting an XUV photon.

$I_p$ is the ionization potential and

$$U_p = \frac{e^2E^2}{4\,m\omega^2} \propto I\lambda^2 \tag{2}$$

is the ponderomotive energy of the electron [137] in the laser field oscillating with angular frequency $\omega$. Here, $e$ and $m$ denote electron charge and mass respectively, $I$ is the laser intensity and $\lambda$ the wavelength. Although very simple, this cut-off law agrees well with experimental findings and predicts similar results as the quantum mechanical description [134]. In particular, it describes the well-known linear scaling of the cut-off energy with laser intensity and the quadratic scaling with wavelength.

Classical electron trajectory analysis also reveals that more than one electron trajectory can contribute to the emission of each harmonic. While electrons that tunnel during the first half of the laser half cycle (assuming that the field cycle starts at the zero crossing of the sinusoidal laser field) will be accelerated away from the ion (see figure 4(b)), electrons born during the second half define two different classes of trajectories, usually referred to as *short* and *long*, reflecting their excursion times. Both, short and long trajectories can lead to photon energies $I_p \leqslant \epsilon_{ph} \leqslant \epsilon_{ph}^{max}$. Note that, although less likely, even longer trajectories exist, involving one or multiple electron rescattering events. The excursion of the electron in the continuum and the time of return defines a phase of the emitted XUV photon, the dipole phase [138].

Due to the coherence of the HHG process, the wide spectral width that a typical HHG spectrum spans can support attosecond pulses in the time domain. For isotropic nonlinear media and sinusoidal laser pulses, two attosecond pulses are formed per laser cycle and electron trajectory. Their duration can reach from several 100 as directly after emission down to below 100 as after temporal compression, which is usually done via transmission through a dispersive metallic filter [139].

### 3.2. An introduction to macroscopic effects in HHG

We here give a brief introduction to basic principles of coherent wave superposition and macroscopic effects relevant to HHG in gases, following closely [29]. We start by briefly discussing *coherent* and *phase-matched* emission. The focus of this section lies on effects arising from phase-mismatches between the generated XUV field and the fundamental laser field and includes re-absorption of the generated XUV radiation in the nonlinear medium. The introduction disregards spatiotemporal pulse re-shaping and group velocity mismatch effects, which can occur at very high laser intensities, dense nonlinear media and large spectral bandwidths. However, such effects are fully included in the macroscopic scaling discussion presented in section 4.

*3.2.1. Basic principles of coherent wave superposition.* The emission of XUV light via HHG is a coherent process. If we disregard perturbations that might occur e.g. due to intensity fluctuations or due to varying imperfections in the laser beam spatial profile, the relative phase of the XUV radiation emitted from different atoms within the nonlinear medium or at different times within the duration of the driving laser pulse, will not change. Consequently, depending on the driving laser characteristics, a high spatial and temporal coherence of the emitted XUV light can be expected. If the laser repetition rate and the carrier envelope offset frequency are stabilized, high temporal coherence can even be achieved between consecutive laser pulses. Remarkably, the highest coherence time for XUV radiation measured today, generated via HHG, exceeds 1 s [12].

For coherent light emission, the number of emitted photons scales quadratically with the number of single atom emitters if the relative phase of the XUV light emitted from different locations within the nonlinear medium stays constant when the number of atoms is changed. This basic principle can be expressed as:

$$S_q \propto \rho^2 S_{\Delta\phi}. \tag{3}$$

Here, $S_q$ denotes the generated harmonic signal of harmonic order $q$, $1 \geqslant S_{\Delta\phi} \geqslant 0$ is a function that accounts for phase-matching and re-absorption of the emitted XUV light in the nonlinear medium and $\rho$ is the gas density. $S_{\Delta\phi} = 1$ describes fully phase-matched generation under the absence of re-absorption, (i.e. all emitted photons are coherently added in phase) while $S_{\Delta\phi} = 0$ corresponds to fully destructive interference. The process scales as $S_q \propto \rho^2$ if $S_{\Delta\phi}$ does not change with $\rho$. A quadratic growth of $S_q$ confirms the coherence of the HHG process but does not indicate phase-matched generation [140]. In contrast, as will be shown in the next subsections, phase-matched generation is usually achieved in conditions where $S_{\Delta\phi}$ depends on the gas density, thus implying a deviation from perfect quadratic growth of $S_q$ with density.

*3.2.2. Phase matching in HHG.* As in low-order frequency mixing processes, most efficient frequency conversion can be expected when the wave vector of the generated field matches the sum of the generating field vectors. We here consider the wave vectors defined by the carrier wave of the fundamental and the harmonic fields and a corresponding wave vector mismatch[6] $\Delta\mathbf{k}(q) = q\mathbf{k} - \mathbf{k}_q$. A generalization for

[6] Note that the wave vector mismatch is sometimes defined with different sign.

**Table 1.** Signs, corresponding refractive index and phase velocity comparison for the four wave vector mismatch components present in non-guiding HHG schemes. Here, $c$ denotes the vacuum speed of light. The laser focus is located at $z = 0$.

| | Sign | Refractive indices | Phase velocities |
|---|---|---|---|
| $\Delta k_g$, focusing | Negative | | $c_1 > c_q > c$ |
| $\Delta k_d$, dipole | Negative, for $z < 0$<br>Positive, for $z > 0$ | | |
| $\Delta k_n$, neutral | Positive | $n_1 > 1 > n_q$ | $c_1 < c < c_q$ |
| $\Delta k_p$, plasma | Negative | $n_1^e < n_q^e < 1$ | $c_1 > c_q > c$ |

continuous XUV emission is easily possible by using a continuous representation of the wave vector. For HHG in gases, $\Delta\mathbf{k}(q)$ changes usually slowly with frequency, thus group velocity mismatch effects can often be neglected.

For a non-guiding generation scheme defined e.g. via a focused Gaussian laser beam, the wave vector mismatch between the $q$th harmonic field and the induced polarization at frequency $q\omega_0$ can be expressed as a sum of four terms [141, 142]:

$$\Delta\mathbf{k} = \Delta\mathbf{k}_g + \Delta\mathbf{k}_d + \Delta\mathbf{k}_n + \Delta\mathbf{k}_p, \tag{4}$$

with $\Delta\mathbf{k}_g$ denoting the wave vector mismatch due to the Gouy phase, $\Delta\mathbf{k}_d$ is the wave vector mismatch induced by the dipole phase, which arises from the frequency- and intensity-dependent electron trajectory in the continuum. Further, $\Delta\mathbf{k}_n$ and $\Delta\mathbf{k}_p$ account for dispersion in the neutral gas medium and the generated plasma, respectively. A possible wave vector mismatch due to the nonlinear refractive index is neglected for HHG in gases as for typical generation conditions this contribution is small compared to the terms listed above. The four terms can be defined as (we omit vector notation for the sake of simplicity and consider a Gaussian laser beam propagating along the optical axis $z$):

$$\Delta k_g = -q\frac{\partial}{\partial z}\left[\zeta(z) - \frac{kx^2}{2R(z)}\right]_{x,\, z\to 0} - \frac{q}{z_R}, \tag{5}$$

$$\Delta k_d = \alpha(q)\frac{\partial I}{\partial z}, \tag{6}$$

$$\Delta k_n = q\frac{\omega}{c}(n_1 - n_q), \tag{7}$$

$$\Delta k_p = q\frac{\omega}{c}(n_1^e - n_q^e). \tag{8}$$

Here, $\zeta(z) = \mathrm{atan}(z/z_R)$ denotes the Gouy phase shift for the fundamental beam with Rayleigh length $z_R$ and beam radius of curvature $R(z)$. Following common practice, the dipole phase is approximated as proportional to the laser intensity $I$ with $\alpha(q)$ denoting a proportionality constant [138]. This simple approximation is usually sufficient for individual harmonic orders but does not provide the correct relative phase across the harmonic spectrum. The refractive index for the fundamental laser field in the neutral gas, $n_1$, can be approximated via the static polarizability of the gas $\alpha_{dip}$ as $n_1 \approx 1 + N_0\alpha_{dip}/\epsilon_0$ [143], where $N_0$ and $\epsilon_0$ denote the density of neutral atoms and the vacuum permittivity, respectively. Tabulated values for the corresponding harmonic refractive index $n_q$ can be found for example in [144]. The plasma refractive index is given by $n_q^e = \sqrt{(1 - N_e/N_c)}$ where $N_e$ denotes the free electron density and $N_c = \epsilon_0 m\omega^2/e^2$ is the critical density beyond which the plasma becomes opaque to electromagnetic radiation of frequency $\omega$. An overview of the four components showing their signs as well as the corresponding phase velocities of the fundamental ($c_1$) and harmonic ($c_q$) waves (from [29]) is provided in table 1.

The rather complicated dependence of the four phase mismatch components on different generation parameters such as focusing geometry, gas density and intensity implies large temporal and spatial variations of $\Delta\mathbf{k}$. For HHG, phase-matched generation can therefore usually only be achieved transiently in time and within part of the generation volume. Consequently, phase-matched generation does not necessarily correspond to a globally maximized photon flux and can typically be achieved for a rather large range of generation parameters. This is different from many low-order frequency conversion processes in crystals where temporal and spatial variations of the phase matching conditions can often be neglected, leading to a narrow parameter range for which phase matching can be achieved.

*3.2.3. Pressure-induced phase-matching.* For optimizing HHG, the gas density is a very important parameter as it controls dispersion in the partially ionized medium thus allowing the adjustment of $\Delta k_{n,p}$ to compensate for the wave vector mismatch introduced by the Gouy phase and the dipole phase [140]. Rewriting equation (4) and assuming $\Delta k_d \approx 0$ (generation in the focus or for short trajectory harmonics), we obtain [117]:

$$p_{match}\left[\frac{\partial\Delta k_n}{\partial p} + \frac{\partial\Delta k_p}{\partial p}\right] + \Delta k_g = 0. \tag{9}$$

Here, the wave vector mismatch caused by dispersion is rewritten as $\Delta k_{n,p} = p \cdot \partial\Delta k_{n,p}/\partial p$, the partial derivatives being independent on pressure[7].

Equation (9) defines a phase-matching pressure $p_{match}$ and can be used to illustrate important principles for phase-matching of HHG. As $\Delta k_g < 0$, the equation has a physical solution only for $|\Delta k_n| > |\Delta k_p|$, i.e. the ionization level has to be below a critical value $\eta_{crit}$, which is typically a few percent for most noble gases, near infrared driving lasers and photon

[7] For simplicity, we do not distinguish explicitly between gas pressure and density, assuming a constant gas temperature for pressure/density dependent phenomena.

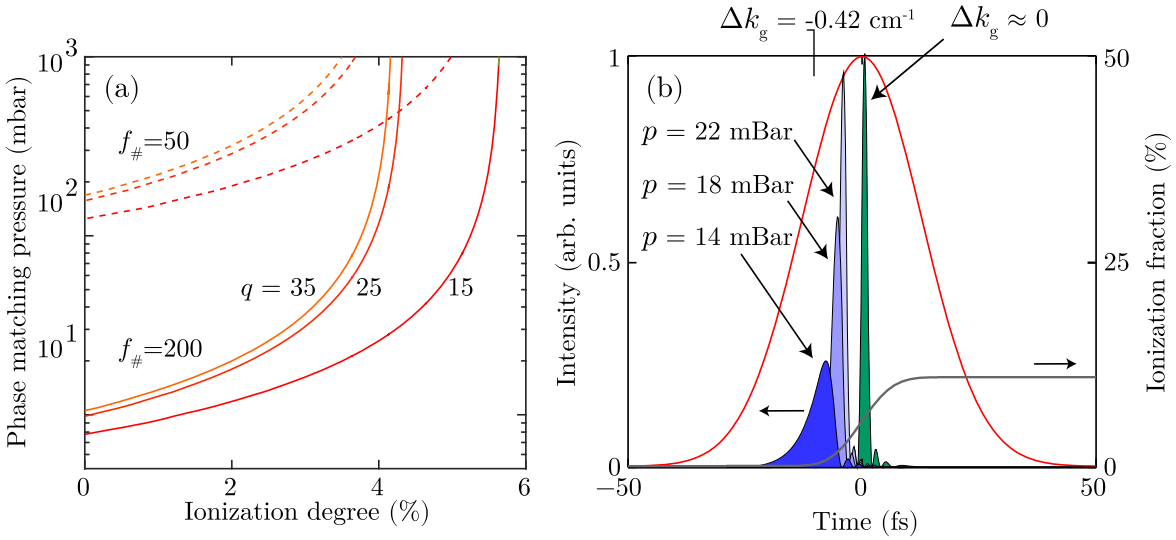


**Figure 5.** Simulation of pressure-induced phase matching in argon for an 800 nm driving laser field: (a) phase matching pressure as a function of ionization level for different focusing geometries (defined via the *f*-number $f_{\#}$) and harmonic orders. (b) Harmonic intensity ($q = 21$) as a function of time showing clear signatures of pressure induced transient phase matching, for $\Delta k_g \neq 0$ (blue peaks) and $\Delta k_g = 0$ (green peak). The peak intensity was chosen to reach $\eta_{crit}$ approximately at the pulse center. The red line depicts the laser field intensity, the gray line the cycle-averaged ionization fraction.

energies in the spectral region around ∼20–100 eV. Figure 5(a) shows $p_{match}$ for argon as a function of the ionization level for two different focusing geometries. At low ionization, $p_{match}$ is defined by $\Delta k_g$ and $\Delta k_n$ and depends only weakly on the harmonic order. Consequently, a relatively large bandwidth can be phase-matched [27]. As the ionization level approaches $\eta_{crit}$, $p_{match}$ increases rapidly, showing a strong spectral dependence. As the laser pulse passes through the nonlinear medium, the ionization level increases and a transient phase matching behavior can be observed. Phase-matched generation occurs early at the leading edge of the pulse for low gas densities while a high gas density shifts the maximum emission to later times and higher intensities, leading to shorter temporal confinement, as illustrated in figure 5(b). For the special case of $\Delta k_g \approx 0$, equation (9) predicts phase-matched generation independent on the gas density when the ionization level reaches $\eta_{crit}$. The simulations shown in figure 5(b) are based on a simple one-dimensional model. For HHG in a three-dimensional gas medium, longitudinal and radial intensity variations lead to a less transient behavior of the total emitted HHG signal.

*3.2.4. Phase-matched and absorption limited HHG.* Although phase matching in HHG is a complicated spatially inhomogeneous and dynamical process, the basic principles can nicely be illustrated using a simple one-dimensional model. The generated signal in a static medium of length $L$ is the coherent sum over all single atom emitters and can be written as:

$$S_q \propto \left| d_q \int_0^L \mathrm{d}z \exp[\mathrm{i}(\Delta k + \mathrm{i}\kappa_q)(L - z)] \right|^2 \tag{10}$$

$$= |d_q|^2 \mathrm{e}^{-\kappa_q L} \cdot \frac{\cosh(\kappa_q L) - \cos(\Delta k L)}{\Delta k^2 + \kappa_q^2}. \tag{11}$$

Here, $d_q$ denotes the $z$-dependent dipole amplitude for harmonic order $q$ and $\kappa_q$ is the absorption coefficient. Equation (11) is formally identical to equation (1) in [120] with $\Delta k$ and $\kappa_q$ being replaced by the coherence length $L_{coh} = \pi/\Delta k$ and the absorption length $L_{abs} = 1/2\kappa_q$. For $\kappa_q \to 0$, $S_q$ shows the well-known sinc-function behavior for frequency conversion processes in the absence of absorption.

Following [120] we illustrate in figure 6(a) the main principles for optimizing macroscopic effects for HHG in an absorbing medium. The ideal case for most efficient frequency conversion occurs when $\kappa_q = 0$ and $\Delta k = 0$. In this case, the harmonic signal increases quadratically with medium length (dashed line in figure 6(a)). For HHG in a gaseous medium, $\kappa_q \neq 0$ and depending on the magnitude of $L_{coh}$, $S_q$ approaches different limits for increasing medium length. It can be shown that at least half of the maximum conversion efficiency obtained for absorption-limited generation is reached when $L_{coh} \geqslant 2\pi L_{abs}$ and $L_{med} \geqslant 3L_{abs}$, as indicated by the green area in figure 6(a).

An extension of these simple principles allows a direct comparison between two well-known generation schemes for HHG: the non-guiding gas medium (gas cell) and the guiding capillary. The gas cell is simple to implement but sets limits on the maximum coherence length whereas the capillary-based approach is technically more challenging but offers the advantage of a more or less unlimited coherence length. An approximate comparison of the performance of both schemes can be obtained with the help of equations (9) and (11). Assuming that there are no constraints on the medium length, equation (11) can be simplified [141]:

$$S_q/S_q^{max} \underset{L_{med}\to\infty}{\longrightarrow} \frac{1}{1 + 4\pi^2 \frac{L_{abs}^2}{L_{coh}^2}}. \tag{12}$$

This equation describes the asymptotic value of $S_q$, visible in

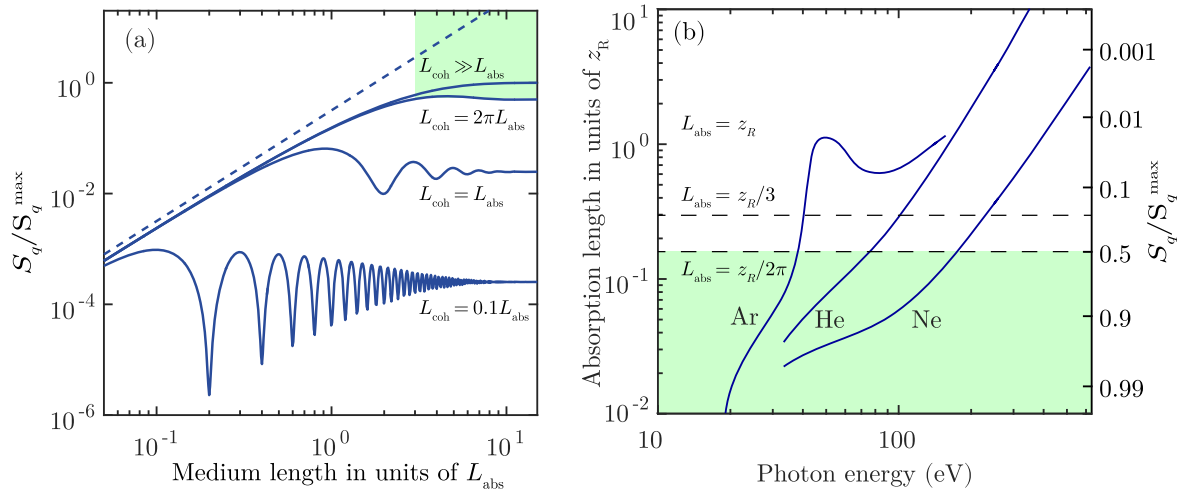


**Figure 6.** (a) Harmonic signal $S_q$ as a function of the absorption length $L_{abs}$ for different coherence lengths $L_{coh}$, normalized to the maximum absorption limited signal $S_q^{max}$ at $L_{coh} \gg L_{abs}$. Inspired by [120]. The dashed line indicates absorption-free HHG. (b) XUV-absorption length as a function of photon energy for different gases for $\lambda = 800$ nm. The gas density was chosen to maximize $L_{coh}$ for each photon energy. The right vertical axis (nonlinear scale) indicates the maximum harmonic signal for a non-guiding generation scheme $S_q$ with $L_{coh} = z_R$, normalized to the maximum absorption limited signal in a guided configuration $S_q^{max}$ with $L_{coh} \gg L_{abs}$. In both figure panels, the green shading marks the parameter range for which $S_q/S_q^{max} \geqslant 0.5$.

figure 6(a), normalized to the maximum absorption limited signal $S_q^{max}$ for $L_{med} \gg L_{abs}$. Here $S_q/S_q^{max}$ depends only on the ratio $L_{abs}/L_{coh}$. For HHG in a non-guiding geometry, we approximate the maximum coherence length as $L_{coh} \approx z_R$. Due to the nonlinear variation of the laser intensity, the dipole phase and the Gouy phase along $z$, even for optimized gas density, a much longer coherence length is usually not realistic. For a defined $z_R$ and a given XUV photon energy (or harmonic order), equation (9) provides an optimum pressure and thus, a corresponding absorption length $L_{abs}(q)$ can be calculated. Figure 6(b) shows $L_{abs}(q)$ for different gases as a function of photon energy. We show $L_{abs}(q)$ in units of $z_R$ taking into account that $z_R \propto 1/p_{match} \propto L_{abs}$, thus making the diagram valid for all focusing geometries and gas densities. Via equation (12), $L_{abs}(q)$ can directly be linked to a relative harmonic signal $S_q/S_q^{max}$ that can be generated for $L_{abs} = L_{abs}(q)$ and $L_{coh} = z_R$. As this signal is normalized to the corresponding absorption limited signal for unlimited coherence length $S_q^{max}$, it provides a direct measure for the maximum absorption limited signal that can be expected for a non-guiding generation scheme (gas cell) in comparison with the guiding scheme (capillary) for the same generation pressure. As phase-matched generation inside a guiding geometry can require slightly different gas densities compared to free focus HHG [62], quantitative deviations from the displayed trends can be expected. It should also be noted that the coupling of the driving laser beam into the capillary is usually not perfect and beating between multiple capillary modes can cause intensity variations and thus reduce the coherence length.

The green area in figure 6(b) indicates the regime for which our simple model predicts that non-guided HHG is at least half as efficient as the guided scenario. For argon, this is the case for XUV photon energies below ~40 eV, while for helium and neon the threshold photon energies are ~75 eV and ~180 eV. These values are obtained assuming a low ionization fraction ($\Delta k_p = 0$). For ionization fractions approaching the critical ionization level, equation (9) predicts an increased phase-matching pressure and thus a shorter absorption length, causing the threshold photon energies to shift to higher values. In this case, a less severe difference between the free-focus HHG and the guided geometry can be expected. Note that the figure provides the relative signal strength independently for each gas type but cannot be used for a comparison of the absolute signals of different gases. Our simple estimate agrees well with the trend visible in figure 3 as a comparison between different XUV sources based on non-guided and guided HHG does not show a clear advantage for the guided scheme at low photon energies up to ~100 eV while capillary-based sources clearly dominate above 200 eV.

## 4. Scaling pulse energy, repetition rate and average power of HHG-based XUV sources

The wide range of available parameters makes HHG-based XUV sources versatile tools in many areas. Some applications, however, demand different source parameters and naturally call for an extension of existing parameter regimes thus motivating the investigation of scaling laws and limitations. Well-known examples discussed in detail in the literature are the scaling of the HHG-process with driving wavelength [58, 60–62] and the scaling of the harmonic cut-off e.g. with intensity [133]. While driving wavelength scaling concepts towards longer wavelength have mostly been employed to increase the cut-off photon energy, the scaling to shorter wavelength as realized e.g. via cascaded harmonic generation, has recently attracted attention as a power scaling concept [110, 111].

Since the early days of HHG, several groups have reported investigations of pulse energy and average power scaling approaches involving focal length and nonlinear medium length scaling (see e.g. [117, 118, 145–147]). Recently, a very general scaling concept was identified, explaining how the nonlinear medium and the focusing geometry as well as the gas density have to be scaled with input laser pulse energy in order to allow the invariant scaling of the HHG process and other nonlinear optical phenomena in gases [28]. In this section, we review in detail this scaling concept and its implications for HHG-based XUV and attosecond sources. Although our discussion concentrates on a parameter scaling with input laser pulse energy, the scaling concept is much more versatile, allowing the invariant scaling of repetition rate[8] and average power provided that suitable laser sources are available. While for a constant laser average power an increasing laser pulse energy implies a decreasing repetition rate, the development of higher average power driving laser sources enables to increase the average power of HHG-based XUV sources by applying pulse energy scaling concepts (see also figure 3).

### 4.1. From Maxwell's equations to universal scaling laws

*4.1.1. Derivation of the wave equation.* Here, we follow a general approach based on nonlinear wave equations (see e.g. [148] for an introduction to nonlinear wave equations). We start with two of the most fundamental equations describing light–matter interactions, the Maxwell–Faraday and the Maxwell–Ampre equation, belonging to the well-known Maxwell equations in matter:

$$\nabla \times \mathbf{E} = -\frac{\partial \mathbf{B}}{\partial t}, \tag{13}$$

$$\nabla \times \mathbf{B} = \mu_0 \left( \mathbf{J} + \frac{\partial \mathbf{D}}{\partial t} \right). \tag{14}$$

Here, $\mathbf{E}$, $\mathbf{B}$, $\mathbf{D}$ and $\mathbf{J}$ denote electric field, magnetic field, electric displacement and the current density of free charges, respectively. The constant $\mu_0$ denotes the vacuum permeability. All field variables are functions describing an amplitude and a phase, which depend on space and time. Here, we omit the explicit notation of these dependencies. For practical reasons, wave equations are often written in the frequency domain. We follow this convention and start the derivation of the wave equation directly in the frequency domain. A field variable $\mathbf{F}(t)$ can be transformed from the time into the frequency domain via a Fourier transform: $\hat{\mathbf{F}}(\omega) = \mathcal{F}[\mathbf{F}(t)] = \int_{-\infty}^{\infty} \exp(\mathrm{i}\omega t)\mathbf{F}(t)\mathrm{d}t$. Using further the property $\mathcal{F}[\partial^n \mathbf{F}(t)/\partial t^n] = (\mathrm{i}\omega)^n \hat{\mathbf{F}}(\omega)$, equations (13) and (14) become:

$$\nabla \times \hat{\mathbf{E}} = -\mathrm{i}\omega \hat{\mathbf{B}}, \tag{15}$$

$$\nabla \times \hat{\mathbf{B}} = \mu_0 (\hat{\mathbf{J}} + \mathrm{i}\omega \hat{\mathbf{D}}). \tag{16}$$

Taking now the curl of equation (15) allows us to combine equations (15) and (16), leading to:

$$\nabla \times (\nabla \times \hat{\mathbf{E}}) = \mu_0 (-\mathrm{i}\omega \hat{\mathbf{J}} + \omega^2 \hat{\mathbf{D}}). \tag{17}$$

The electric displacement is a function of the polarization $\hat{\mathbf{P}}$:

$$\hat{\mathbf{D}}(\omega) = \epsilon_0 \epsilon(\omega) \hat{\mathbf{E}}(\omega) + \hat{\mathbf{P}}(\omega), \tag{18}$$

where $\epsilon_0$ and $\epsilon(\omega) = 1 + \chi(\omega)$ are vacuum and relative permittivity and where $\chi(\omega)$ denotes the susceptibility of the medium. Note that in our notation, $\hat{\mathbf{P}}$ denotes the nonlinear polarization. The linear polarization is included in $\epsilon(\omega)$. Inserting equation (18) into (17) and identifying the refractive index $n^2 = \epsilon$ and the vacuum speed of light $c = (\mu_0 \epsilon_0)^{-1/2}$ leads to:

$$\nabla \times (\nabla \times \hat{\mathbf{E}}) - \frac{n^2 \omega^2}{c^2} \hat{\mathbf{E}} = \mu_0 (\omega^2 \hat{\mathbf{P}} - \mathrm{i}\omega \hat{\mathbf{J}}). \tag{19}$$

For simplicity reasons and without loss of generality, we formally redefine the polarization to include the free charge current $\hat{\mathbf{P}} - \mathrm{i}\hat{\mathbf{J}}/\omega \rightarrow \hat{\mathbf{P}}$. Using the relation $\nabla \times (\nabla \times \hat{\mathbf{E}}) = \nabla(\nabla \cdot \hat{\mathbf{E}}) - \nabla^2 \hat{\mathbf{E}}$ and identifying the wave number $k = n\omega/c$ we obtain:

$$\nabla^2 \hat{\mathbf{E}} - \nabla(\nabla \cdot \hat{\mathbf{E}}) + k^2 \hat{\mathbf{E}} = -\mu_0 \omega^2 \hat{\mathbf{P}}. \tag{20}$$

Up to this point no approximation has been made and equation (20) constitutes a very general nonlinear wave equation which directly follows from Maxwell's equations. Most propagation phenomena within linear and nonlinear optics, however, allow a few basic approximations which simplify the above equation. First, we can neglect the second term on the left-hand side of equation (20). This is possible if all field vectors are oriented perpendicularly to the propagation direction (along $z$), which is valid for not too tight focusing geometries (numerical aperture $\lesssim 0.3$). Second, we assume linear polarization, allowing us to transform the above equation into a scalar equation:

$$\nabla^2 \hat{E} + k^2 \hat{E} = -\mu_0 \omega^2 \hat{P}. \tag{21}$$

Third, if propagation in only one direction is considered (again, this is sufficient for most linear and nonlinear propagation phenomena), another simplification is possible. Separating the Laplace operator into a longitudinal and a transverse component ($\nabla^2 = \Delta_\perp + \partial^2/\partial z^2 = \Delta_\perp + \partial_z^2$) allows us to factorize equation (22) by using the forward and backward propagators $\partial_z \pm \mathrm{i}k$ [149]:

$$(\partial_z + \mathrm{i}k)(\partial_z - \mathrm{i}k)\hat{E} = -\Delta_\perp \hat{E} - \mu_0 \omega^2 \hat{P}. \tag{22}$$

When neglecting the right-hand side of this equation (diffraction and nonlinear propagation), it is easy to see that the remaining equation describes the superposition of two counter propagating plane waves, i.e. $(\partial_z \pm \mathrm{i}k)\hat{E} = 0$. Neglecting the backward propagating solution is formally equivalent to the approximation $[\partial_z + \mathrm{i}k] \approx 2\mathrm{i}k$ [148], leading to a well-known uni-directional propagation equation, the Forward–Maxwell equation [150]:

$$\left( \partial_z - \frac{\mathrm{i}}{2k} \Delta_\perp - \mathrm{i}k \right) \hat{E} = \frac{\mathrm{i}\omega}{2nc\epsilon_0} \hat{P}. \tag{23}$$

This equation is a very general paraxial wave equation and

[8] We here consider repetition rates low enough to allow the nonlinear gas medium to be replenished between consecutive laser pulses.

can be used to describe nonlinear wave and pulse propagation provided they are linearly polarized and not too tightly focused. As no approximations have been made on the bandwidth, this equation does not set any limitations on the duration of the pulses under consideration. Different nonlinearities such as harmonic generation, self-phase modulation or even complex processes such as filamentation can be taken into account via the nonlinear polarization $\hat{P}$, which can be a sum of different polarization terms.

*4.1.2. Scaling linear wave propagation.* We introduce our scaling model by considering light propagation in vacuum, i.e. $\hat{P} = 0$ and $k = \omega/c$:

$$\left(\partial_z - \frac{\mathrm{i}}{2k}\Delta_\perp - \mathrm{i}\frac{\omega}{c}\right)\hat{E} = 0. \tag{24}$$

While the first two terms in this equation describe wave propagation and diffraction, the third term defines the spatial carrier wave with wavelength $\lambda = 2\pi c/\omega$, propagating at the speed of light in vacuum $c$. For most optical propagation phenomena, the absolute location of the spatial carrier wave is not important (in contrast to the temporal carrier wave, usually referred to as the carrier-envelope offset, discussed below). We can therefore remove the third term on the left-hand side by introducing the field $\hat{\mathcal{E}} \equiv \hat{E}\exp[-\mathrm{i}\omega z/c]$:

$$\left(\partial_z - \frac{\mathrm{i}}{2k}\Delta_\perp\right)\hat{\mathcal{E}} = 0. \tag{25}$$

The change from $\hat{E}$ to $\hat{\mathcal{E}}$ corresponds to a transformation of equation (24) from the laboratory frame to a frame moving at the vacuum speed of light $c$ [151]. The variable $z$ now denotes the longitudinal position in the moving frame of reference. In this reference frame, the spatial carrier wave is a constant, non-moving wave. It is important to note that the above transformation is not equivalent to the usual slowly varying envelope approximation that sets limits on the spectral bandwidth, and consequently pulse duration.

Equation (25) describes the propagation of both monochromatic waves and short pulses. A prominent solution to this equation that can nicely introduce our scaling principles, is the Gaussian beam that propagates under the influence of diffraction. If $\hat{\mathcal{E}}_\mathrm{G}(z, r, \omega)$ describes such a beam and is thus a solution of equation (25), any other field $\hat{\mathcal{E}}_{\eta\mathrm{G}}(\eta^2 z, \eta r, \omega)$, with $\eta$ denoting a scaling parameter, is a solution as well, describing a spatially scaled version of $\hat{\mathcal{E}}_\mathrm{G}(z, r, \omega)$. Equation (25) is thus scale-invariant under the transformation:

$$z \longrightarrow \eta^2 z, \tag{26}$$

$$r \longrightarrow \eta r. \tag{27}$$

This scaling behavior is well represented by characteristic parameters of a Gaussian beam, as for example Rayleigh length $z_\mathrm{R}$ and focal spot radius $W_0$, which show the following, well-known scaling behavior:

$$z_\mathrm{R} \longrightarrow \eta^2 z_\mathrm{R}, \tag{28}$$

$$W_0 \longrightarrow \eta W_0. \tag{29}$$

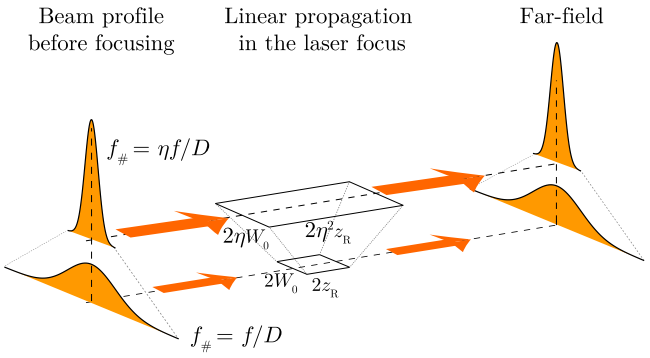


**Figure 7.** Scaling linear wave propagation: a focused Gaussian beam retains its Gaussian shape upon propagation through the focus into the far-field. The same characteristic propagation phenomena can be expected at tighter or looser focusing, i.e. the characteristic beam parameters follow our scaling principles.

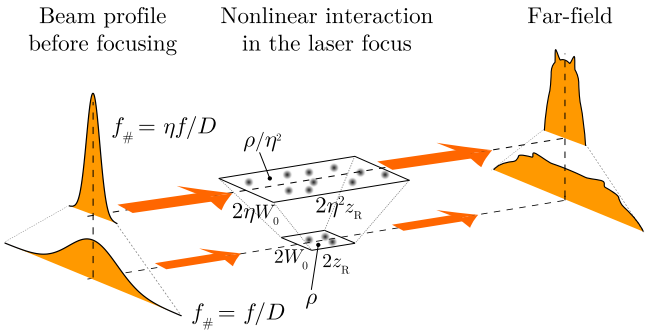


**Figure 8.** Scaling nonlinear wave propagation: a focused Gaussian beam can be reshaped spatially, spectrally and temporally upon propagation through a nonlinear medium. The same characteritic propagation phenomena can be expected at tighter or looser focusing, if the focusing geometry, the nonlinear medium dimensions, the gas density as well as the input laser power (or pulse energy for pulsed lasers) are scaled correctly. In this case, the characteristic beam parameters follow our scaling principles even for nonlinear beam propagation.

In practice, a laser beam can be easily scaled by simply changing the focusing geometry, as shown in figure 7. Note that in this illustration, only the beam diameter before focusing $D$ (not the focal length) was changed. Reducing $D$ at a constant distance $f$ before the focus by a factor of $\eta$ and increasing the laser pulse energy at the same time by $\eta^2$ results in a larger focal spot but constant peak intensity within the focus region.

*4.1.3. Scaling nonlinear wave propagation.* These basic and simple scaling principles can be extended to nonlinear wave propagation, if gas density $\rho$ and laser pulse energy $\epsilon_\mathrm{in}$ are included as scaling parameters (see also figure 8). To illustrate this, we reintroduce dispersion via $k = n\omega/c$ and nonlinear polarization $\hat{\mathcal{P}} \equiv \hat{P}\exp[-\mathrm{i}\omega z/c]$ into equation (25) and obtain a modified version of equation (23), written for the moving frame of reference:

$$\left(\partial_z - \frac{\mathrm{i}}{2k}\Delta_\perp - \mathrm{i}K\right)\hat{\mathcal{E}} = \frac{\mathrm{i}\omega^2}{2kc^2\epsilon_0}\hat{\mathcal{P}}, \tag{30}$$

with $K = k - \omega/c$. Neglecting the weak pressure dependence of $1/k$ and taking into account the approximately linear dependence of dispersion phenomena in gases on the gas density, i.e. $K \propto \rho$, renders the left-hand side of equation (30) scale-invariant if the gas density is added as a scaling parameter:

$$\rho \longrightarrow \rho/\eta^2. \tag{31}$$

Finally, an appropriate scaling of the laser pulse energy

$$\epsilon_{\text{in}} \longrightarrow \eta^2 \epsilon_{\text{in}} \tag{32}$$

ensures that the electrical field amplitude stays constant upon scaling, implying that the right side of equation (30) follows the same scaling relation as the left side for all nonlinear interaction for which the polarization scales linearly with density. Interestingly, for nonlinear propagation phenomena relevant for HHG in gases such as harmonic generation, multiphoton absorption and even for the Kerr effect, the nonlinear polarization scales approximately linearly with gas density. For a detailed discussion on the approximations made to obtain a fully scale-invariant nonlinear propagation equation, the reader is referred to the supplementary material of [28]. Limitations of the scaling model are discussed in section 4.4. In the discussion below, perfect scalability of equation (30) is assumed.

*4.1.4. Consequences for HHG.* Equation (30) is a general nonlinear wave equation that can be used to describe the propagation of the fundamental driving laser field as well as of the generated harmonic fields. This can be done for example, in a two-step process. First, the fundamental field is propagated through the nonlinear medium. The fundamental field defines the nonlinear polarization $\hat{\mathcal{P}}_{\text{h}}(\hat{\mathcal{E}}) = 2d_{\text{h}}(\hat{\mathcal{E}})\rho$, the source term for the generated harmonic field $\hat{\mathcal{E}}_{\text{h}} \equiv \hat{E}_{\text{h}} \exp[-\text{i}\omega z/c]$, with $\omega$ now describing the harmonic frequencies. Here $d_{\text{h}}$ is the single atom nonlinear dipole moment. Second, the generated harmonic field is propagated through the medium. The nonlinear wave equation for the harmonic field reads as:

$$\left(\partial_z - \frac{\text{i}}{2k}\Delta_\perp - \text{i}K\right)\hat{\mathcal{E}}_{\text{h}} = \frac{\text{i}\omega^2}{2kc^2\epsilon_0}\hat{\mathcal{P}}_{\text{h}}(\hat{\mathcal{E}}). \tag{33}$$

A complete separation of the propagation of fundamental and harmonic fields via equations (30) and (33) is possible when back-conversion of the generated harmonic fields to fundamental frequencies as well as any influence of the harmonic field on the HHG process can be neglected. Further, the spectral components of fundamental and harmonic fields must not overlap. As equation (33) does not set any limits on the spectral bandwidth considered, all fields (including the fundamental laser field) can alternatively be propagated using a single equation. The above steps are introduced for pedagogical reasons and can be of practical relevance depending on the numerical methods applied. For a detailed discussion about the numerical techniques available to solve nonlinear propagation equations the reader is referred to [148].

The above discussion on the scalability of nonlinear wave equations has far reaching consequences for HHG-based XUV sources. Scale-invariance of the fundamental field propagation ensures a scale-invariant dipole response of the nonlinear medium. Further, as both fundamental and harmonic fields obey scale-invariant equations, the phase difference between both fields $\Delta\varphi$, determining the macroscopic buildup of the HHG signal, is scale-invariant. This also applies for possible group-delays [152] between generated and generating fields. The consequence is scale-invariance for both the single atom response as well as the macroscopic response of the nonlinear medium. In practice, a generation configuration characterized by a set of experimentally accessible parameters (laser pulse properties, focusing geometry, nonlinear medium properties) can be arbitrarily up-and within certain limits down-scaled to other pulse energies (see section 4.4) without changing the characteristic properties of the frequency conversion processes involved, and in particular the conversion efficiency.

Our scaling concept has recently been verified experimentally using the example of femtosecond laser pulse filamentation in gases, see [28]. As the main propagation phenomena determining HHG such as dispersion in the partially ionized medium, self-phase modulation and plasma defocusing as well as multiphoton absorption are present in the filamentation process, this experimental demonstration has direct implications also for processes like HHG, confirming the validity of our scaling concept. In addition, the experimental trend shown in figure 3, with most of the experimental results for a certain photon energy range lying on constant average power diagonal lines, is a clear expression of the scaling. In particular, for high repetition rate HHG our scaling formalism has enabled to boost the conversion efficiency for single-pass HHG sources to values close to the best values reported for high-pulse energy systems [86, 118].

For HHG in general and especially for IAP generation, the carrier-envelope phase of the driving laser pulse can critically influence the generation process. However, CEP changes arise due to linear and nonlinear propagation effects as e.g. dispersion in the partially ionized medium, effects that are scale-invariant within our scaling laws. This can be qualitatively understood considering that the extension of the length of the nonlinear medium is compensated by a decreased medium density. This implies that the CEP is a scale-invariant parameter and thus, even CEP-dependent phenomena can be easily up- or downscaled.

*4.1.5. Possibilities enabled by the scale-invariance.* The scaling model described in the previous sections does first of all provide a simple recipe for scaling a given generation scenario defined by the laser input pulse energy, the focusing geometry, the medium length and density to other laser pulse energies. This allows us to easily adapt high-harmonic and attosecond sources to new parameter regimes provided by

today's and future laser technology. It further provides a general scaling framework for various nonlinear optical processes in gases, finding application for example in femtosecond laser filamentation [28].

Aside from providing a practical scaling recipe, the concept of scale-invariance sheds new light on macroscopic effects in HHG. Through the scaling relations provided for laser pulse energy $\epsilon_{\text{in}}$, focal length[9] $f$ and gas density $\rho$, these parameters are implicitly linked. This allows us to describe macroscopic effects in HHG as independent of one of these three parameters. If we, for example, take $f$ as a scaling parameter, a given generation scenario can be found for all[10] $f$ as long as $\epsilon_{\text{in}}$ and $\rho$ are scaled correctly. An implication is that phase-matching effects are not necessarily dependent on $f$-as discussed in [117, 118], see also figure 6(b), which illustrates that absorption limited HHG does not depend on the focal length. Note that this statement might seem to contradict equation (4). However, a simple normalization of the spatial dimension allows us to avoid this apparent contradiction. In general, minimizing the number of independent parameters in a complex problem by normalization can greatly simplify simulations and is a well-known concept for multi-dimensional simulations. The parameter space can be reduced by introducing dimensionless quantities [153], i.e. by normalizing simulation parameters to other characteristic quantities.

Scale-invariance has another interesting implication for HHG. If for example technical limitations arise for a given HHG scenario, a scaled configuration might allow avoiding these limitations while providing otherwise identical characteristics. For example, several studies investigate the concept of quasi-phase matching in HHG by designing a nonlinear medium with alternating gases [127]. However, matching the gas medium length to the characteristic length set by the coherence length can be technically very challenging at focusing geometries typically employed for HHG where the coherence length can be short. In contrast, in an up-scaled configuration the coherence length can be increased without changing any characteristic properties of the HHG process but allowing the use of longer nonlinear media.

### 4.2. User friendly examples and guidelines

The scaling relations derived in section 4.1 are summarized below. In the derivation presented above, we introduced the parameter $\eta$ as an arbitrary, dimensionless scaling parameter. In practice, it is often more convenient to express the scaling relations using the laser pulse energy as a scaling parameter. Both approaches are presented in table 2. While the scaling model predicts the scaling of both, radial and longitudinal dimensions, simplified scaling relations can be derived for conditions where the nonlinear interaction happens only close to the laser focus but not in the near-field close to the focusing element. To ensure a global invariant scaling, laser beam diameter before focusing $D$ and focal length $f$ have to be scaled as $D \propto \eta$ and $f \propto \eta^2$. In practice, to ensure scale-invariance for nonlinear interactions in or close to the laser focus, which is determined by $f_{\#} = f/D$, it is sufficient to keep $D$ as an invariant parameter upon scaling and scale the focal length as $f \propto \eta$. In both cases, the characteristic dimensions of the laser focus scale in the same way. For HHG in capillaries (see section 4.3.1), the capillary diameter $d$ has to be added as scaling parameter.

**Table 2.** Overview of the relations that allow scaling HHG and attosecond pulse generation with parameter $\eta$ and input laser pulse energy $\epsilon_{\text{in}}$ while keeping the characteristic properties of the frequency conversion process invariant.

| Parameter | Global scaling | | Focus scaling | |
|---|---|---|---|---|
| | Scaling with $\eta$ | Scaling with $\epsilon_{\text{in}}$ | Scaling with $\eta$ | Scaling with $\epsilon_{\text{in}}$ |
| $\epsilon_{\text{in}}$ | $\eta^2$ | — | $\eta^2$ | — |
| $f$ | $\eta^2$ | $\epsilon_{\text{in}}$ | $\eta$ | $\sqrt{\epsilon_{\text{in}}}$ |
| $D$ | $\eta$ | $\sqrt{\epsilon_{\text{in}}}$ | constant | constant |
| $d$ | $\eta$ | $\sqrt{\epsilon_{\text{in}}}$ | $\eta$ | $\sqrt{\epsilon_{\text{in}}}$ |
| $L$ | $\eta^2$ | $\epsilon_{\text{in}}$ | $\eta^2$ | $\epsilon_{\text{in}}$ |
| $\rho$ | $1/\eta^2$ | $1/\epsilon_{\text{in}}$ | $1/\eta^2$ | $1/\epsilon_{\text{in}}$ |

Below we list parameters, that need to be kept constant upon scaling to allow scale-invariance as well as parameters that are found to be scale-invariant as a consequence:

Scale-invariant input parameters: wavelength $\lambda$, pulse duration $\tau$, gas type

Scale-invariant output parameters: laser focus intensity, conversion efficiency $\epsilon_q/\epsilon_{\text{in}}$ ($\epsilon_q$ denotes the pulse energy of a single harmonic), laser pulse CEP, temporal pulse structure, spectral pulse structure, spatial pulse structure normalized to laser divergence

An example for HHG scaling illustrating the parameter ranges over which invariant scaling is possible, is presented in figure 9. We start by a typical scenario for HHG in argon, using the following input parameters, marked with a vertical solid line in figure 9(b): $\tau = 10$ fs, $\epsilon_{\text{in}} = 1$ mJ, $p = 16$ mbar, $W_0 = 42.4$ $\mu$m, $L = 32$ mm. This basic configuration is then up- and down-scaled applying the scaling relations presented in table 2 for focus-scaling. The intensity distribution for both, down- and up-scaled spatially and temporally resolved attosecond pulse trains is displayed in (a) and (c), respectively, for three positions within the nonlinear medium. The formation of attosecond pulse trains and their evolution along the nonlinear medium can be clearly seen. The extreme generation conditions chosen for this simulation lead in both cases, (a) and (c), to strong spatio-temporal laser pulse distortions and thus to a reduced on-axis emission for $t > 0$. The simulations include both laser and XUV field propagation effects, for details see supplementary information of [28] and [154, 155]. The dipole response was calculated using the strong field approximation (SFA) [134]. As predicted by the scaling-model, an almost perfect scaling-behavior can be

[9] We here simply name the focal length as the spatial scaling parameter, assuming a constant beam diameter before focusing and a medium length scaled according to the scaling model as $L \propto f$, see also section 4.2.

[10] Within the paraxial limit.

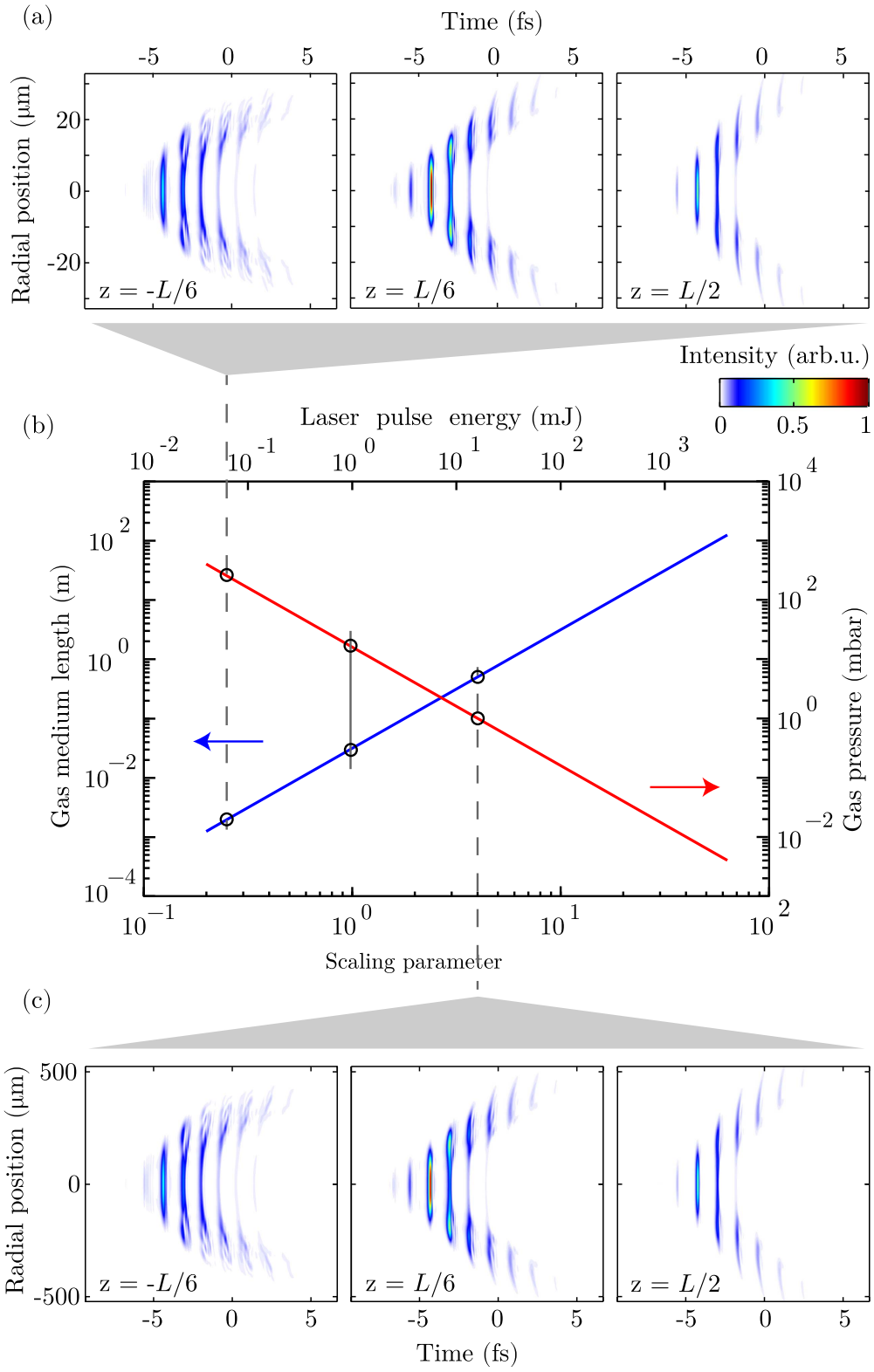


**Figure 9.** Simulated spatiotemporal intensity distributions for high-harmonic emission (above 31.5 eV) in argon at three positions within the nonlinear medium. The employed parameters are: (a) $\tau = 10$ fs, $\epsilon_{\text{in}} = 62.5$ $\mu$J, $p = 256$ mbar, $W_0 = 10.6$ $\mu$m, $L = 2$ mm, and (c): $\tau = 10$ fs, $\epsilon_{\text{in}} = 16$ mJ, $p = 1$ mbar, $W_0 = 169.6$ $\mu$m, $L = 0.51$ m. In (b), laser pulse energy, gas-medium length and gas pressure are indicated. The solid lines indicate the scaling of the displayed parameters according to the scaling model. Reproduced with permission from [28].

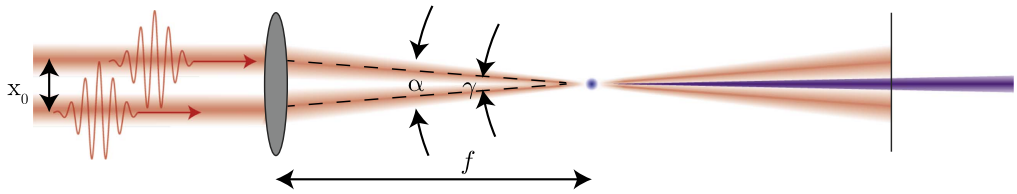


**Figure 10.** Schematic illustration of NCHHG.

observed, in this example with an input pulse energy ratio of 256. The solid lines in (b) indicate the scaling of medium length, laser pulse energy and gas pressure within and beyond the parameter range (e.g. to laser pulse energies above 1 J) used in the simulations.

### 4.3. Scaling different generation geometries

*4.3.1. Guided geometries.* A well known alternative approach to gas jet or cell-based HHG sources is the capillary-based scheme in which the laser pulse is coupled into a guiding capillary [62, 156]. As discussed above, this approach can lead to a longer coherence length for the HHG process and can thus, depending on gas type and photon energy, lead to an increased conversion into the XUV.

For capillary-based HHG, the fundamental laser pulse is guided, leading to different propagation characteristics compared to non-guided propagation with in particular an approximately constant intensity over a large distance. In contrast to the propagation of the laser pulse, the propagation of the XUV radiation is not affected by the capillary. Recently, Böhle and co-workers [157] have identified similar scaling principles as described above for laser pulse propagation in hollow capillaries.

For sufficiently large capillary diameters where dispersion due to the guiding and propagation losses in the capillary can be neglected, the laser pulse propagation can indeed be scaled invariantly using the above scaling relations. Consequently, the same scaling principles can be applied for HHG in capillaries. However, upper scaling limits can arise due to technical difficulties arising for producing straight large-scale capillaries and for the coupling of high energy laser pulses with typically increased beam pointing fluctuations into a capillary.

*4.3.2. Noncollinear geometries.* During recent years, noncollinear generation geometries have attracted increasing attention for HHG [158–160] and attosecond pulse generation [103, 161, 162]. Most of them employ relatively small angles between the driving laser beams, thus, allowing a complete description of the underlying wave propagation phenomena using paraxial approximations as e.g. equation (30). In practice, for propagation simulations that do not require a cylindrical symmetry, starting with defining the input laser pulse as a set of spatially separated and tilted input pulses allows us to propagate both pulses simultaneously. Applying the scaling relations listed in table 2, will ensure scale-invariance for sufficiently small noncollinear angles. To ensure that paraxial effects are negligible, the numerical aperture NA $= \sin(\alpha)$ (see figure 10) of the covered beam angle $\alpha$ should be less than 0.3.

An important parameter for noncollinear HHG (NCHHG) is the noncollinear angle, which can be defined as $\sin(\gamma/2) = (x_0/2)/f$ or simply $\gamma \approx x_0/f$ with $x_0$ denoting the beam separation before focusing. Scaling $x_0$ and $f$ according to the scaling relations leads to:

$$\gamma \longrightarrow \gamma/\eta. \tag{34}$$

If the geometrical scaling is realized by simply changing $f$ and keeping the beam diameter constant (see section 4.2), NCHHG scale invariance can be obtained by keeping also $x_0$ constant and simply scaling $f$ together with density and input pulse energy. In other words, although NCHHG is known to depend critically on $\gamma$ [163], the characteristics for NCHHG do not change if both $\gamma$ and $f$ are scaled appropriately.

### 4.4. Limitations

The scaling model discussed in section 4.1 is generally valid over a large parameter range. Remarkably, the model does not indicate a fundamental upper limit although technical limitations may occur. Those include length limitations for usual table-top XUV-sources as well as limitations set by the available laser pulse parameters (e.g. because of a typically decreased spatial beam quality for high pulse energy lasers). In the other direction, towards decreasing laser pulse energy, several limitations can arise. First of all, scale-invariance as described via equation (30) is only valid within the paraxial approximation, implying limitations at very tight focusing geometries. In practice, this limit is usually only reached with microscope objective focusing, which is not easily applicable for HHG with short laser pulses. Second, minor approximations have to be made in order to reach full scale-invariance of equation (30). These include neglecting the weak density dependence of $1/k$ as well as assuming that $K$ and $\mathcal{P}$ vary linearly with pressure. Both approximations are usually very good (see also the discussion in the supplementary information of [28]) but deviation can occur at very high gas densities. Finally, many-body interactions such as cluster formation, avalanche ionization as well as a possible influence of neighboring atoms for multi-photon ionization [164] and HHG [130, 168] can lead to deviations from $\mathcal{P} \propto \rho$, especially for high densities and long driving wavelength.

## 5. Summary and outlook

As discussed in section 2.3, today's HHG-based XUV sources reach 1 mW levels of average power in a single harmonic

order around 20 eV, with a spectral brightness approaching the parameter ranges available at modern synchrotron facilities at comparable photon energies [24]. These remarkable parameters indicate the potential of today's HHG-based technology to surpass many limits set by a low photon flux. An even further increased photon flux will greatly aid current applications of HHG-based XUV sources and might open new application areas as e.g. in the semiconductor industry or within life sciences.

Recent trends indicate source development efforts especially along two lines: towards higher XUV pulse energies to allow the study of nonlinear processes driven by ultra-short XUV pulses [26, 97–99, 115] and towards higher repetition rates. In both cases, higher average power values are desirable. Towards higher repetition rates, the main driving applications are the measurement of electronic processes on surfaces and in solid-state samples [106–108], frequency comb spectroscopy of atoms and ions [6] and experiments involving coincidence detection [166]. Here, two sub-directions can be identified: single-pass HHG sources driven by high-power, fiber-based laser systems [167] or oscillators [94] and intra-cavity HHG approaches [37, 38, 101].

For the production of intense XUV pulses, suitable driving laser sources that could in principle allow further HHG upscaling beyond the 10 $\mu$J level per harmonic order[11] are already available, however, so far mostly at very low repetition rates (typically a few Hz). Current efforts, as undertaken for example for the Extreme Light facility ELI-ALPS aim to reach 100 mJ level few-cycle laser pulses at high repetition rate (1 kHz). HHG source scaling concepts as discussed in this tutorial, are needed to adapt common attosecond source concepts to these newly available parameter regimes. Besides the scaling model discussed in section 4.1, other concepts involving very high density but short nonlinear gas media as well as HHG in a converging or diverging laser beam are being discussed. However, while the scaling concept presented in this tutorial provides a complete recipe for the invariant up-scaling of well-explored HHG-source regimes, other approaches will have to be tested first and their performance has yet to be demonstrated.

For single-pass HHG-based sources operating at high average power levels and multi-MHz repetition rates, the consistent application of the scaling relations presented in this tutorial together with important advances for the corresponding driving laser technology has only recently allowed to increase XUV-average power levels by orders of magnitude [23, 118]. Further laser development is needed to push the available average power to even higher levels [168]. During recent years, fiber-based high-power laser systems in combination with novel pulse post-compression schemes have contributed major advances [86]. Similarly, laser schemes employing OPCPA could boost few-cycle laser pulses to new pulse-energy levels [167]. Further advances along these lines and possibly in combination with coherent combining and pulse stacking approaches [169] will open again new parameter regimes for HHG and attosecond science.

Finally, XUV sources based on driving the HHG process inside a femtosecond enhancement cavity have opened a new high-repetition rate regime and can compete very well with the average power values of single-pass sources (see figure 3). Similarly as for single-pass sources, further advances for high-power driving laser systems in combination with improved high-power mirror technology will enable further power-scaling. However, in addition to these routes that will also greatly benefit single-pass HHG sources, even without increasing the pumping power levels further, enhancement-cavity approaches can benefit from improved control of the nonlinear dynamics inside the enhancement cavity [24, 131, 170]. At the same time, the rigorous application of down-scaling concepts promises to allow phase-matched HHG inside an optical cavity. Taken together, these approaches can allow pushing the average power levels of intra-cavity based HHG sources further, promising new possibilities for ultrahigh precision spectroscopy in the VUV and XUV [171], possibly opening the door for the direct measurement and control of energetic atomic or even nuclear transitions [172]. Applications within attosecond science will also benefit from further power scaling advances for intra-cavity HHG, especially in combination with new attosecond pulse gating approaches [103, 162] which might bring IAP sources into the multi-100 MHz regime.

[11] This estimate assumes a conversion efficiency of $10^{-5}$ as reported for Ti:sapphire based laser systems [27, 120] and a laser pulse energy above 1J.

## Acknowledgments

This research was supported by the Swedish Research Council, the European Research Council (PALP) and the Knut and Alice Wallenberg Foundation. The authors would also like to thank Katalin Kovacs, Valer Tosa, Emeric Balogh and Katalin Varjú for discussions and numerical simulations of HHG and filamentation scaling as well as Piotr Rudawski, Bastian Manschwetus, Sylvain Maclot and Per Johnsson for their input regarding HHG scaling.

## References

[1] Ott C, Kaldun A, Raith P, Meyer K, Laux M, Evers J, Keitel C, Greene C and Pfeifer T 2013 *Science* **340** 716
[2] Bertrand J, Wörner H, Salières P, Villeneuve D and Corkum P 2013 *Nat. Phys.* **9** 174
[3] Mansson E *et al* 2014 *Nat. Phys.* **10** 207
[4] Calegari F *et al* 2014 *Science* **346** 336
[5] Hassan M *et al* 2016 *Nature* **530** 66
[6] Cingöz A, Yost D, Allison T, Ruehl A, Fermann M, Hartl I and Ye J 2012 *Nature* **482** 68
[7] Zürch M, Foertsch S, Matzas M, Pachmann K, Kuth R and Spielmann C 2014 *J. Med. Imaging* **1** 031008
[8] Bellini M, Lynga C, Tozzi A, Gaarde M, Hänsch T, L'Huillier A and Wahlström C G 1998 *Phys. Rev. Lett.* **81** 297
[9] Lyna C, Gaarde M, Delfin C, Bellini M, Hänsch T, L'Huillier A and Wahlström C G 1999 *Phys. Rev.* A **60** 4823

[10] Salières P, L'Huillier A, Antoine P and Lewenstein M 1999 *Adv. At. Mol. Opt. Phys.* **41** 83
[11] Terschlüsen J, Asgaker M, Svanqvist M, Plogmaker S, Nordgren J, Rubensson J E, Siegbahn H and Söderström J 2014 *Nucl. Instrum. Methods Phys. Res.* A **768** 84
[12] Benko C, Allison T, Cingöz A, Hua L, Labaye F, Yost D and Ye J 2014 *Nat. Photon.* **8** 530
[13] Popmintchev T *et al* 2012 *Science* **336** 1287
[14] Silva F, Teichmann M S, Cousin S L, Hemmer M and Biegert J 2015 *Nat. Commun.* **6** 6611
[15] Calegari F, Sansone G, Stagira S, Vozzi C and Nisoli M 2016 *J. Phys. B: At. Mol. Opt. Phys.* **49** 062001
[16] Eckle P, Pfeiffer A, Cirelli C, Staudte A, Dörner R, Muller H, Böttiker M and Keller U 2008 *Science* **322** 1525
[17] Schultze M *et al* 2010 *Science* **328** 1658
[18] Dahlström J, L'Huillier A and Maquet A 2012 *J. Phys. B: At. Mol. Phys.* **45** 183001
[19] Ozawa A, Zhao Z, Kuwata-Gonokami M and Kobayashi Y 2015 *Opt. Express* **23** 15107–18
Kandula D Z, Gohle C, Pinkert T J, Ubachs W and Eikema K S E 2010 *Phys. Rev. Lett* **105** 063001
[20] Schwenke J, Mai A, Miranda M, He X, Genoud G, Mikkelsen A, Pettersson S G, Persson A and L'Huillier A 2008 *J. Mod. Opt.* **55** 2723–30
[21] Zürch M, Rothhardt J, Hädrich S, Demmler S, Krebs M, Limpert J, Tünnermann A, Guggenmos A, Kleineberg U and Spielmann C 2014 *Sci. Rep.* **4** 7356
[22] Miao J, Ishikawa T, Robinson I and Murnane M 2015 *Science* **348** 530
[23] Rothhardt J, Hädrich S, Demmler S, Tschernajew M, Klas R, Tünnermann A and Limpert J 2016 *Proc. of High Intensity Lasers and High Field Phenomena (Long Beach, CA)* (Optical Society of America) HM6B.5
[24] Benko C 2016 *PhD Thesis* University of Colorado, Boulder
[25] Carstens H *et al* 2016 *Optica* **3** 366–9
[26] Takahashi E, Lan P, Mücke O, Nabekawa Y and Midorikawa K 2013 *Nat. Commun.* **4** 2691
[27] Rudawski P *et al* 2013 *Rev. Sci. Instrum.* **84** 073103
[28] Heyl C M *et al* 2016 *Optica* **3** 75
[29] Heyl C M 2014 *PhD Thesis* Lund University and University of Marburg (https://lup.lub.lu.se/search/publication/fc34da91-a11c-4d96-9ff9-59b194ad898)
[30] McPherson A, Gibson G, Jara H, Johann U, Luk T S, McIntyre I A, Boyer K and Rhodes C K 1987 *J. Opt. Soc. Am.* B **4** 595
[31] Ferray M, L'Huillier A, Li X F, Lompré L A, Mainfray G and Manus C 1988 *J. Phys.* B **21** L31
[32] Farkas G and Tóth C 1992 *Phys. Lett.* A **168** 447–50
[33] Harris S, Macklin J and Hänsch T 1993 *Opt. Commun.* **100** 487–90
[34] Paul P, Toma E, Breger P, Mullot G, Auge F, Balcou P, Muller H and Agostini P 2001 *Science* **292** 1689
[35] Hentschel M, Kienberger R, Spielmann C, Reider G, Milosevic N, Brabec T, Corkum P, Heinzmann U, Drescher M and Krausz F 2001 *Nature* **414** 509
[36] Seres J, Seres E, Verhoef A, Tempea G, Streli C, Wobrauschek P, Yakovlev V, Scrinzi A, Spielmann C and Krausz F 2005 *Nature* **433** 7026
[37] Jones R, Moll K, Thorpe M and Ye J 2005 *Phys. Rev. Lett.* **94** 193201
[38] Gohle C, Udem T, Herrmann M, Rauschenberger J, Holzwarth R, Schuessler H, Krausz F and Hänsch T 2005 *Nature* **436** 234
[39] Rundquist A, Durfee C III, Chang Z, Herne C, Backus S, Murnane M and Kapteyn H 1998 *Science* **280** 1412
[40] Tsakiris G, Eidmann K, Meyer-ter Vehn J and Krausz F 2006 *New J. Phys.* **8** 19
[41] Ghimire S, Dichiara A, Sistrunk E, Agostini P, Dimauro L and Reis D 2011 *Nat. Phys.* **7** 138
[42] Wirth A *et al* 2011 *Science* **334** 195
[43] Mourou G, Mironov S, Khazanov E and Sergeev A 2014 *Eur. Phys. J.: Spec. Top.* **223** 1181
[44] Miyazaki K and Sakai H 1992 *J. Phys. B: At. Mol. Opt. Phys.* **25** L83–9
[45] Balcou P, Cornaggia C, Gomes A S L, Lompre L A and L'Huillier A 1992 *J. Phys. B: At. Mol. Opt. Phys.* **25** 4464–85
[46] Crane J K, Falcone R W, Perry M D and Herman S 1992 *Opt. Lett.* **17** 1256–8
[47] Moulton P F 1986 *J. Opt. Soc. Am.* B **3** 125–33
[48] Spence D E, Kean P N and Sibbett W 1991 *Opt. Lett.* **16** 42–4
[49] Strickland D and Mourou G 1985 *Opt. Commun.* **56** 219–21
[50] Macklin J J, Kmetec J D and Gordon C L 1993 *Phys. Rev. Lett.* **70** 766–9
[51] Kondo K, Sarukura N, Sajiki K and Watanabe S 1993 *Phys. Rev.* A **47** R2480–3
[52] L'Huillier A, Lewenstein M, Salières P, Balcou P, Ivanov M Y, Larsson J and Wahlström C G 1993 *Phys. Rev.* A **48** R3433–6
[53] Wahlström C G, Larsson J, Persson A, Starczewski T, Svanberg S, Salières P, Balcou P and L'Huillier A 1993 *Phys. Rev.* A **48** 4709–20
[54] Nisoli M, De Silvestri S, Svelto O, Szipocs R, Ferencz K, Spielmann C, Sartania S and Krausz F 1997 *Opt. Lett.* **22** 522
[55] Xu L, Hänsch T W, Spielmann C, Poppe A, Brabec T and Krausz F 1996 *Opt. Lett.* **21** 2008–10
[56] Gaarde M B, Antoine P, Persson A, Carré B, L'Huillier A and Wahlström C G 1996 *J. Phys. B: At. Mol. Opt. Phys.* **29** L163
[57] Shan B and Chang Z 2001 *Phys. Rev.* A **65** 011804
[58] Colosimo P *et al* 2008 *Nat. Phys.* **4** 386–989
[59] Schmidt B E, Shiner A D, Giguère M, Lassonde P, Trallero-Herrero C A, Kieffer J C, Corkum P B, Villeneuve D M and Légaré F 2012 *J. Phys. B At. Mol. Opt. Phys.* **45** 074008
[60] Tate J, Auguste T, Muller H G, Salières P, Agostini P and DiMauro L F 2007 *Phys. Rev. Lett.* **98** 013901
[61] Shiner A, Trallero-Herrero C, Kajumba N, Bandulet H C, Comtois D, Legare F, Gignure M, Kieffer J C, Corkum P and Villeneuve D 2009 *Phys. Rev. Lett.* **103** 073902
[62] Popmintchev T, Chen M C, Bahabad A, Gerrity M, Sidorenko P, Cohen O, Christov I, Murnane M and Kapteyn H 2009 *Proc. Natl Acad. Sci. USA* **106** 10516
[63] Dubietis A, Butkus R and Piskarskas A P 2006 *IEEE J. Sel. Top. Quantum Electron.* **12** 163–72
[64] Witte S and Eikema K S E 2012 *IEEE J. Sel. Top. Quantum Electron.* **18** 296–307
[65] Dubietis A, Jonusauskas G and Piskarskas A 1992 *Opt. Commun.* **88** 437–40
[66] Fattahi H *et al* 2014 *Optica* **1** 45–63
[67] Limpert J, Klenke A, Kienel M, Breitkopf S, Eidam T, Hädrich S, Jauregui C and Tuennermann A 2014 *IEEE J. Sel. Top. Quantum Electron.* **20** 5
[68] Schulz M *et al* 2011 *Opt. Lett.* **36** 2456–8
[69] Metzger T, Schwarz A, Teisset C Y, Sutter D, Killi A, Kienberger R and Krausz F 2009 *Opt. Lett.* **34** 2123–5
[70] Witte S, Zinkstok R, Hogervorst W and Eikema K 2005 *Opt. Express* **13** 4903–8
[71] Fuji T, Ishii N, Teisset C Y, Gu X, Metzger T, Baltuska A, Forget N, Kaplan D, Galvanauskas A and Krausz F 2006 *Opt. Lett.* **31** 1103–5
[72] Mücke O D *et al* 2009 *Opt. Lett.* **34** 118–20
[73] Rothhardt J *et al* 2010 *Opt. Express* **18** 12719–26
[74] Andriukaitis G, Balčiūnas T, Ališauskas S, Pugžlys A, Baltuška A, Popmintchev T, Chen M C, Murnane M M and Kapteyn H C 2011 *Opt. Lett.* **36** 2755–7

[75] Biegert J, Bates P K and Chalus O 2012 *IEEE J. Sel. Top. Quantum Electron.* **18** 531
[76] Matyschok J *et al* 2013 *Opt. Express* **21** 29656–65
[77] Matyschok J *et al* 2012 *Opt. Lett.* **37** 933
[78] Shamir Y, Rothhardt J, Hädrich S, Demmler S, Tschernajew M, Limpert J and Tünnermann A 2015 *Opt. Lett.* **40** 5546–9
[79] Hädrich S, Rothhardt J, Krebs M, Tavella F, Willner A, Limpert J and Tünnermann A 2010 *Opt. Express* **18** 20242–50
[80] Krebs M, Hädrich S, Demmler S, Rothhardt J, Zaïr A, Chipperfield L, Limpert J and Tünnermann A 2013 *Nat. Photon.* **7** 555
[81] Rudawski P *et al* 2015 *Eur. Phys. J.* D **69** 1–6
[82] Boullet J, Zaouter Y, Limpert J, Petit S, Mairesse Y, Fabre B, Higuet J, Mével E, Constant E and Cormier E 2009 *Opt. Lett.* **34** 1489–91
[83] Hädrich S, Krebs M, Rothhardt J, Carstens H, Demmler S, Limpert J and Tünnermann A 2011 *Opt. Express* **19** 19374–83
[84] Lorek E, Larsen E, Heyl C M, Carlström S, Palacek D, Zigmantas D and Mauritsson J 2014 *Rev. Sci. Instrum.* **85** 123106
[85] Travers J C, Chang W, Nold J, Joly N Y and Russell P S J 2011 *J. Opt. Soc. Am.* B **28** A11–26
[86] Hädrich S, Krebs M, Hoffmann A, Klenke A, Rothhardt J, Limpert J and Tünnermann A 2015 *Light Sci. Appl.* **4** 93
[87] Rothhardt J, Hädrich S, Klenke A, Demmler S, Hoffmann A, Gotschall T, Eidam T, Krebs M, Limpert J and Tünnermann A 2014 *Opt. Lett.* **39** 5224
[88] Chiang C T, Blattermann A, Huth M, Kirschner J and Widdra W 2012 *Appl. Phys. Lett.* **101** 071116
[89] Saraceno C J, Emaury F, Heckl O H, Baer C R E, Hoffmann M, Schriber C, Golling M, Südmeyer T and Keller U 2012 *Opt. Express* **20** 23535–41
[90] Brons J, Pervak V, Fedulova E, Bauer D, Sutter D, Kalashnikov V, Apolonskiy A, Pronin O and Krausz F 2014 *Opt. Lett.* **39** 6442–5
[91] Heckl O H, Saraceno C J, Baer C R E, Südmeyer T, Wang Y Y, Cheng Y, Benabid F and Keller U 2011 *Opt. Express* **19** 19142–9
[92] Mak K F, Seidel M, Pronin O, Frosz M H, Abdolvand A, Pervak V, Apolonski A, Krausz F, Travers J C and Russell P S J 2015 *Opt. Lett.* **40** 1238–41
[93] Pronin O, Seidel M, Lücking F, Brons J, Fedulova E, Trubetskov M, Pervak V, Apolonski A, Udem T and Krausz F 2015 *Nat. Commun.* **6** 6988
[94] Emaury F, Diebold A, Saraceno C and Keller U 2015 *Optica* **2** 980
[95] Kienberger R *et al* 2004 *Nature* **427** 817
[96] Schultze M, Goulielmakis E, Uiberacker M, Hofstetter M, Kim J, Kim D, Krausz F and Kleineberg U 2007 *New J. Phys.* **9** 243
[97] Tzallas P, Charalambidis D, Papadogiannis N, Witte K and Tsakiris G 2003 *Nature* **426** 267
[98] Nabekawa Y, Hasegawa H, Takahashi E and Midorikawa K 2005 *Phys. Rev. Lett.* **94** 043001
[99] Tzallas P, Skantzakis E, Nikolopoulos L, Tsakiris G and Charalambidis D 2011 *Nat. Phys.* **7** 781
[100] Campi F, Coudert-Alteirac H, Miranda M, Rading L, Manschwetus B, Rudawski P, L'Huillier A and Johnsson P 2016 *Rev. Sci. Instrum.* **87** 023106
[101] Jones R and Ye J 2002 *Opt. Lett.* **27** 1848
[102] Vincenti H and Quéré F 2012 *Phys. Rev. Lett.* **108** 113904
[103] Louisy M *et al* 2015 *Optica* **2** 563
[104] Kroon D *et al* 2014 *Opt. Lett.* **39** 2218
[105] Rohwer T *et al* 2011 *Nature* **471** 490
[106] Haarlammert T and Zacharias H 2009 *Curr. Opin. Solid State Mater. Sci.* **13** 13
[107] Chiang C T, Huth M, Tritzschler A, Schumann F, Kirschner J and Widdra W 2015 *J. Electron Spectrosc. Relat. Phenom.* **200** 15
[108] Cilento F, Crepaldi A, Manzoni G, Sterzi A, Zacchigna M, Bugnon P, Berger H and Parmigiani F 2016 *J. Electron Spectrosc. Relat. Phenom.* **207** 7
[109] Mills A, Hammond T, Lam M and Jones D 2012 *J. Phys. B: At. Mol. Opt. Phys.* **45** 142001
[110] Popmintchev D *et al* 2015 *Science* **350** 1225
[111] Wang H, Xu Y, Ulonska S, Robinson J, Ranitovic P and Kaindl R 2015 *Nat. Commun.* **6** 7459
[112] Lindner F, Stremme W, Schätzel M, Grasbon F, Paulus G, Walther H, Hartmann R and Strüder L 2003 *Phys. Rev.* A **68** 013814
[113] Lee J, Carlson D and Jones R 2011 *Opt. Express* **19** 23315
[114] Pupeza I *et al* 2013 *Nat. Photon.* **7** 608
[115] Manschwetus B *et al* 2016 *Phys. Rev.* A **93** 061402(R)
[116] Hädrich S, Klenke A, Rothhardt J, Krebs M, Hoffmann A, Pronin O, Pervak V, Limpert J and Tünnermann A 2014 *Nat. Photon.* **8** 779
[117] Heyl C M, Güdde J, L'huillier A and Höfer U 2012 *J. Phys. B: At. Mol. Opt. Phys.* **45** 074020
[118] Rothhardt J, Krebs M, Hädrich S, Demmler S, Limpert J and Tünnermann A 2014 *New J. Phys.* **16** 033022
[119] Cabasse A, Machinet G, Dubrouil A, Cormier E and Constant E 2012 *Opt. Lett.* **37** 4618
[120] Constant E, Garzella D, Breger P, Mével E, Dorrer C, Blanc C L, Salin F and Agostini P 1999 *Phys. Rev. Lett.* **82** 1668
[121] Ding C, Xiong W, Fan T, Hickstein D, Popmintchev T, Zhang X, Walls M, Murnane M and Kapteyn H 2014 *Opt. Express* **22** 6194
[122] Chen M C, Arpin P, Popmintchev T, Gerrity M, Zhang B, Seaberg M, Popmintchev D, Murnane M and Kapteyn H 2010 *Phys. Rev. Lett.* **105** 173901
[123] Cassou K, Daboussi S, Hort O, Guilbaud O, Descamps D, Petit S, MEvel E, Constant E and Kazamias S 2014 *Opt. Lett.* **39** 3770
[124] Hergott J F, Kovacev M, Merdji H, Hubert C, Mairesse Y, Jean E, Breger P, Agostini P, Carré B and Salières P 2002 *Phys. Rev.* A **66** 021801
[125] Takahashi E, Nabekawa Y and Midorikawa K 2002 *Opt. Lett.* **27** 1920
[126] Gauthier D, Guizar-Sicairos M, Ge X, Boutu W, Carré B, Fienup J and Merdji H 2010 *Phys. Rev. Lett.* **105** 093901
[127] Willner A *et al* 2011 *Phys. Rev. Lett.* **107** 175002
[128] Lambert G *et al* 2009 *New J. Phys.* **11** 083033
[129] Vernaleken A *et al* 2011 *Opt. Lett.* **36** 3428
[130] Hädrich S, Rothhardt J, Krebs M, Demmler S, Klenke A, Tünnermann A and Limpert J 2016 *J. Phys. B: At. Mol. Opt. Phys.* **49** 172002
[131] Holzberger S *et al* 2015 *Phys. Rev. Lett.* **115** 023902
[132] Franken P, Hill A, Peters C and Weinreich G 1961 *Phys. Rev. Lett.* **7** 118
[133] Krause J L, Schafer K J and Kulander K C 1992 *Phys. Rev. Lett.* **68** 3535
[134] Lewenstein M, Balcou P, Ivanov M, L'Huillier A and Corkum P 1994 *Phys. Rev.* A **49** 2117
[135] Schafer K J, Yang B, DiMauro L F and Kulander K C 1993 *Phys. Rev. Lett.* **70** 1599
[136] Corkum P 1993 *Phys. Rev. Lett.* **71** 1994
[137] Bucksbaum P H, Freeman R R, Bashkansky M and McIlrath T J 1987 *J. Opt. Soc. Am.* B **4** 760
[138] Lewenstein M, Salières P and L'Huillier A 1995 *Phys. Rev.* A **52** 4747
[139] Zhao K, Zhang Q, Chini M, Wu Y, Wang X and Chang Z 2012 *Opt. Lett.* **37** 3891
[140] Kazamias S, Daboussi S, Guilbaud O, Cassou K, Ros D, Cros B and Maynard G 2011 *Phys. Rev.* A **83** 063405

[141] Kazamias S, Douillet D, Weihe F, Valentin C, Rousse A, Sebban S, Grillon G, Augé F, Hulin D and Balcou P 2003 *Phys. Rev. Lett.* **90** 193901
[142] Gaarde M, Tate J and Schafer K 2008 *J. Phys. B: At. Mol. Opt. Phys.* **41** 132001
[143] Schwerdtfeger P 2008 *Table of Experimental and Calculated Static Dipole Polarizabilities cTCP* (Auckland, New Zealand: Massey University)
[144] Henke B, Gullikson E and Davis J 1993 *At. Data Nucl. Data Tables* **54** 181
[145] L'Huillier A, Schafer K J and Kulander K C 1991 *J. Physics* B **24** 3315–41
[146] Midorikawa K, Nabekawa Y and Suda A 2008 *Prog. Quantum Electron.* **32** 43
[147] Boutu W, Auguste T, Caumes J, Merdji H and Carré B 2011 *Phys. Rev.* A **84** 053819
[148] Couairon A, Brambilla E, Corti T, Majus D, de J Ramirez-Gongora O and Kolesik M 2011 *Eur. Phys. J.: Spec. Top.* **199** 5
[149] Feit M D and Fleck J A 1988 *J. Opt. Soc. Am.* B **5** 633
[150] Husakou A and Herrmann J 2001 *Phys. Rev. Lett.* **87** 203901
[151] Geissler M, Tempea G, Scrinzi A, Schnürer M, Krausz F and Brabec T 1999 *Phys. Rev. Lett.* **83** 2930
[152] Hernández-García C, Popmintchev T, Murnane M M, Kapteyn H C, Plaja L, Becker A and Jaron-Becker A A 2016 *New J. Phys.* **18** 073031
[153] Buckingham E 1914 *Phys. Rev.* **4** 345
[154] Tosa V, Kim H, Kim I and Nam C 2005 *Phys. Rev.* A **71** 063807
[155] Takahashi E, Tosa V, Nabekawa Y and Midorikawa K 2003 *Phys. Rev.* A **68** 238081
[156] Schnurer M, Cheng Z, Sartania S, Hentschel M, Tempea G, Brabec T and Krausz F 1998 *Appl. Phys.* B **67** 263
[157] Böhle F *et al* 2014 *Laser Phys. Lett.* **11** 095401
[158] Bertrand J, Wörner H, Bandulet H C, Bisson A, Spanner M, Kieffer J C, Villeneuve D and Corkum P 2011 *Phys. Rev. Lett.* **106** 023001
[159] Kim K, Zhang C, Shiner A, Kirkwood S, Frumker E, Gariepy G, Naumov A, Villeneuve D and Corkum P 2013 *Nat. Phys.* **9** 159
[160] Negro M, Devetta M, Faccialá D, Ciriolo A, Calegari F, Frassetto F, Poletto L, Tosa V, Vozzi C and Stagira S 2014 *Opt. Express* **22** 29778
[161] Heyl C M, Bengtsson S, Carlström S, Mauritsson J, Arnold C L and Lhuillier A 2014 *New J. Phys.* **16** 052001
[162] Zhong S, He X, Jiang Y, Teng H, He P, Liu Y, Zhao K and Wei Z 2016 *Phys. Rev.* A **93** 033854
[163] Heyl C M, Rudawski P, Brizuela F, Bengtsson S, Mauritsson J and L'Huillier A 2014 *Phys. Rev. Lett.* **112** 143902
[164] Schuh K, Hader J, Moloney J and Koch S 2014 *Phys. Rev.* E **89** 033103
[165] Strelkov V, Platonenko V and Becker A 2005 *Phys. Rev.* A **71** 053808
[166] Ullrich J, Moshammer R, Dorn A, Dörner R, Schmidt L and Schmidt-Böcking H 2003 *Rep. Prog. Phys.* **66** 1463
[167] Hädrich S *et al* 2016 *Appl. Opt.* **55** 1636–40
[168] Kurz H G, Kretschmar M, Binhammer T, Nagy T, Ristau D, Lein M, Morgner U and Kovačev M 2016 *Phys. Rev.* X **6** 031029
[169] Breitkopf S *et al* 2015 *Eur. Phys. J.: Spec. Top.* **224** 2573
[170] Allison T, Cingöz A, Yost D and Ye J 2011 *Phys. Rev. Lett.* **107** 183903
[171] Eyler E, Chieda D, Stowe M, Thorpe M, Schibli T and Ye J 2008 *Eur. Phys. J.* D **48** 43
[172] Kazakov G, Litvinov A, Romanenko V, Yatsenko L, Romanenko A, Schreitl M, Winkler G and Schumm T 2012 *New J. Phys.* **14** 083019
[173] Brizuela F, Heyl C M, Rudawski P, Kroon D, Rading L, Dahlström J, Mauritsson J, Johnsson P, Arnold C L and L'Huillier A 2013 *Sci. Rep.* **3** 1410